Constraints on aerosol sources using GEOS-Chem adjoint and MODIS radiances, and evaluation with multisensor (OMI, MISR) data

Xiaoguang Xu,[1] Jun Wang,[1] Daven K. Henze,[2] Wenjun Qu,[3] and Monika Kopacz[4]

Received 21 December 2012; revised 23 April 2013; accepted 22 May 2013.

[1] We present a new top-down approach that spatially constrains the amount of aerosol emissions using satellite (Moderate Resolution Imaging Spectroradiometer (MODIS)) observed radiances with the adjoint of a chemistry transport model (GEOS-Chem). This paper aims to demonstrate the approach through applying it to a case study that yields the following emission estimates over China for April 2008: 1.73 Tg for SO_2, 0.72 Tg for NH_3, 1.38 Tg for NO_x, 0.10 Tg for black carbon, and 0.18 Tg for organic carbon from anthropogenic sources, which reflects, respectively, a reduction of 33.5%, 34.5%, 18.8%, 9.1%, and 15% in comparison to the prior bottom-up inventories of INTEX-B 2006. The mineral dust emission from the online dust entrainment and mobilization module is reduced by 56.4% of 19.02 to 8.30 Tg. Compared to the prior simulation, the posterior simulation shows a much better agreement with the following independent measurements: aerosol optical depth (AOD) measured by AERONET sun-spectrophotometers and retrieved from Multi-angle Imaging SpectroRadiometer (MISR), atmospheric NO_2 and SO_2 columnar amount retrieved from Ozone Monitoring Instrument (OMI), and in situ data of sulfate-nitrate-ammonium and PM_{10} (particular matter with aerodynamic diameter less than 10 μm) mass concentrations over both anthropogenic pollution and dust source regions. Assuming the bottom-up (prior) anthropogenic emissions are the best estimates for their base year of 2006, the overwhelming reduction in the posterior (top-down) estimate indicates less emission in April 2008 especially for the SO_2 tracer in the central and eastern parts of China, and/or an overestimation in the prior emission. The former is supported by the AOD change detected by MODIS and MISR sensors, while the latter is likely the case for NO_x and NH_3 emissions because no evidence shows that their atmospheric concentration has declined over China. With the promising results shown in this study, continuous efforts are needed toward a holistic and comprehensive inversion of emission using multisensor remote sensing data (of trace gases and aerosols) for constraining aerosol primary and precursor emissions at various temporal and spatial scales.

Citation: Xu, X., J. Wang, D. K. Henze, W. Qu, and M. Kopacz (2013), Constraints on aerosol sources using GEOS-Chem adjoint and MODIS radiances, and evaluation with multisensor (OMI, MISR) data, *J. Geophys. Res. Atmos.*, *118*, doi:10.1002/jgrd.50515.

1. Introduction

[2] Tropospheric aerosols play an important role in the Earth's energy budget and hydrological cycle by directly scattering or absorbing solar radiation (hereafter direct effect) and indirectly altering the cloud microphysical properties and lifetime through serving as cloud condensation nuclei (hereafter indirect effect) [*Haywood and Boucher*, 2000]. The Intergovernmental Panel on Climate Change [*Forster et al.*, 2007] reported direct and indirect aerosol radiative forcing as −0.5 and −0.7 Wm^{-2}, respectively, both with uncertainty of about 100%. Such large uncertainties are attributed not only to a diversity of representations of aerosol microphysical and optical properties across models [*Schulz et al.*, 2006], but also to the uncertainty in the emissions of aerosol particles and aerosol precursors (hereafter aerosol emissions) from both natural and anthropogenic sources. Differences in global aerosol emission estimates, ranging from 22% to over 200% depending on the species, were found among various global chemistry transport models (CTMs) [*Textor et al.*, 2006], highlighting the need to further improve the

[1]Earth and Atmospheric Sciences, University of Nebraska Lincoln, Lincoln, Nebraska, USA.
[2]Mechanical Engineering, University of Colorado Boulder, Boulder, Colorado, USA.
[3]Physical Oceanography Laboratory, Ocean University of China, Qingdao, China.
[4]NOAA Climate Program Office, Silver Spring, Maryland, USA.

Corresponding author: J. Wang, Earth and Atmospheric Sciences, University of Nebraska Lincoln, Lincoln, NE, 68588, USA. (jwang7@unl.edu)

2169-897X/13/10.1002/jgrd.50515

quantifications of aerosol emissions. At regional scales, the emission inventories have much larger uncertainty [*Streets et al*., 2003] and often do not resolve the seasonal or monthly variations, making it difficult to model regional climate, air quality, and visibility. In addition, accurate and timely knowledge of aerosol sources is required for use of air quality models for studying impacts of aerosols on human health [*Pope et al*., 2009].

[3] Current estimates of aerosol emissions are largely based on the "bottom-up" method that integrates diverse information such as fuel consumption in various industries and corresponding measurements of emission rates for different species [*Streets et al*., 2003], economic growth, and the statistics of land use and fire-burned areas [*van der Werf et al*., 2006]. While significant progress has been made [*Streets et al*., 2006], the "bottom-up" approach has a number of limitations. First, the emission inventory (EI) usually has a temporal lag of at least 2 to 3 years, as time is needed to aggregate information from different sources and format them into the emission inventories that are suitable for use in climate models. Second, the temporal resolution of the current EI is usually on monthly to annual scale, which is not sufficient to characterize the daily or diurnal variation of emissions; the aerosol impact on radiative transfer and the variation of cloud properties, however, is often strongly dependent on the time of the day [*Wang et al*., 2006]. Third, the spatial resolutions of the bottom-up emission inventories are usually limited by the availability of the ground-based observations, which often lack the spatial coverage for estimating emission in a uniformly fine resolution for regional modeling of aerosol transport. Finally, bottom-up emission inventories may miss important emission sources that are not well documented including emissions from wild fires, volcanic eruptions, and agricultural activities. All these limitations are amplified over the East Asia region because the economic growth in China is so rapid that information needed for bottom-up approach cannot be timely and reliably documented.

[4] To complement information from bottom-up emissions, remote sensing is increasingly used to better quantify aerosol distributions. The satellite observations and/or products can provide information important for the bottom-up estimate of emissions. Examples include the fire products from Moderate Resolution Imaging Spectroradiometer (MODIS), Advanced Spaceborne Thermal Emission and Reflection Radiometer, and Advanced Very High Resolution Radiometer sensors that are widely used for characterizing the biomass burning emissions [*Borrego et al*., 2008; *van der Werf et al*., 2006, 2010; *Reid et al*., 2009]. Alternatively, the satellite observed tracer abundance could be used to constrain bottom-up estimates of aerosol emissions through the inverse modeling; such method is referred to as a "top-down" constraint. Although satellite-based aerosol retrievals have less precision than in situ measurements, studies have shown that they are able to quantify the atmospheric aerosol loading and temporal variations with good agreement and expected accuracy to the ground-based observations [*Levy et al*., 2010; *Remer et al*., 2005]. Furthermore, the satellite-based aerosol data, in contrast to the ground-based ones, have much higher temporal resolution across the globe. For instance, the MODIS sensor, aboard on NASA's both Terra and Aqua satellites, has a surface footprint size of ~1 km at nadir and needs only 1 to 2 days to achieve global coverage. In addition, the joint retrieval of aerosols from diverse satellite sensors enhances the accuracy of satellite aerosol products [*Sinyuk et al*., 2008], the potential of which has also been shown in the air quality monitoring [*Liu et al*., 2005; *Wang et al*., 2010].

[5] Different top-down techniques have been developed to optimally estimate the emissions from satellite observations, which include but are not limited to the following: (a) the use of a scaling factor that is the ratio of observed tracer abundances to the CTM-simulated counterparts [e.g., *Lee et al*., 2011; *Martin et al*., 2003; *Wang et al*., 2006]; (b) the use of the local sensitivity of change of tracer concentration to the change of emission [e.g., *Lamsal et al*., 2011; *Walker et al*., 2010]; (c) the analytical Bayesian inversion method [e.g., *Heald et al*., 2004]; and (d) the adjoint of CTM [e.g., *Müller and Stavrakou*, 2005; *Henze et al*., 2007, 2009; *Dubovik et al*., 2008; *Kopacz et al*., 2009, 2010; *Wang et al*., 2012]. The first two methods are similar; both assume a linear relationship between model-simulated aerosol abundances and emissions. The analytical method is exact but computationally expensive and thus can only constrain emission in the domain-wise or over coarse spatial resolution [*Kopacz et al*., 2009]. In contrast to the first three approaches, the adjoint approach is designed for exploiting the high density of observations to constrain emission with high resolution [*Kopacz et al*., 2009], as it is able to efficiently calculate gradients of the overall mismatch between observations and model estimates with respect to large sets of parameters (i.e., emissions resolved at each grid box) [*Henze et al*., 2007].

[6] Several studies have successfully analyzed sources of traces gases using the top-down methods, including CO sources from MOPITT sensor over the Asia [*Heald et al*., 2004; *Kopacz et al*., 2009;] and over the globe [e.g., *Stavrakou and Müller*, 2006; *Kopacz et al*., 2010], CO_2 surface flux from the TES sensor [*Nassar et al*., 2011], NO_x emissions from space-based column NO_2 by several satellite sensors [*Lamsal et al*., 2011; *Lin et al*., 2010; *Martin et al*., 2003; *Müller and Stavrakou*, 2005], and SO_2 from SCIAMACHY and Ozone Monitoring Instrument (OMI) sensors [*Lee et al*., 2011], etc. However, not all emissions of trace gases can be *fully* constrained with their satellite-based counterpart products, because some trace gases (e.g., SO_2) can react with other gases (e.g., NH_3), to form either liquid or solid aerosols (e.g., $(NH_4)_2SO_4$). As a result, using measurements of trace gases alone can only provide partial constraints on the emission of the corresponding trace gases.

[7] Ultimately, combined use of measurements of both trace gases and aerosols should provide stronger constraint (than each individual measurement alone) for the emission of aerosols and their precursors including trace gases. Unlike a given trace gas, aerosol has complex chemical composition. Aerosol optical depth (AOD), the only parameter that current satellite remote sensing can provide and is well validated, contains little information on aerosol composition. Consequently, assumption of aerosol composition is often made when using AOD to constrain aerosol models. Examples from previous studies have focused on assimilation of AOD to constrain model AOD [*Wang et al*., 2004; *Zhang et al*., 2008; *Benedetti et al*., 2009], or to estimate $PM_{2.5}$ concentrations [*van Donkelaar et al*., 2006, 2008]. While valuable for forecasts or estimating distribution of

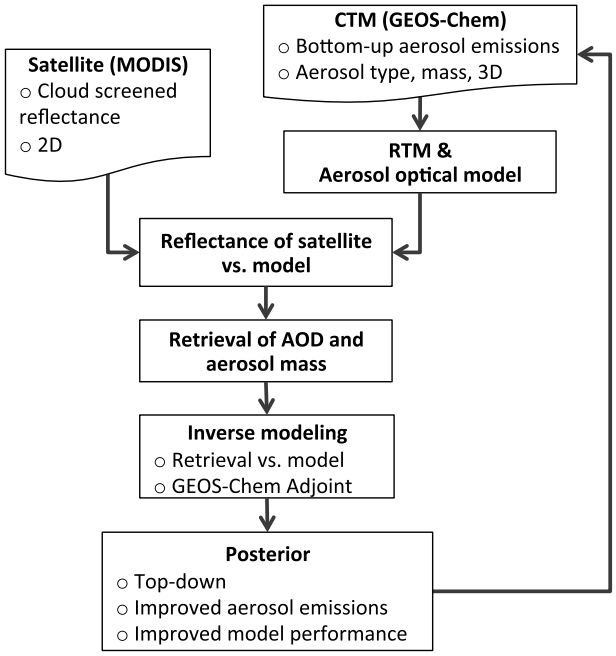

Figure 1. Flowchart of the proposed top-down inversion framework.

aerosols, such studies do not provide direct constraints on aerosol sources. In terms of constraining sources, a recent study by *Dubovik et al*. [2008] constrained aerosol primary sources in single-fine and single-coarse modes, respectively, from MODIS retrieved fine and coarse mode 0.55 μm AOD by inverting the GOCART aerosol transport model. To overcome the inconsistency of aerosol single scattering properties between CTM and aerosol retrieval algorithm that may compromise the use of satellite AOD to quantitatively invert aerosol emissions, *Weaver et al*. [2007] suggested directly assimilating the satellite observed radiance (such as from MODIS) to improve the CTM (GOCART model) simulation of aerosols. Improved retrieval of AOD and improved estimate of surface PM concentration were also obtained by *Drury et al*. [2008] over the U.S. and *Wang et al*. [2010] over China, when the GEOS-Chem-simulated aerosol single scattering properties is used in the retrieval, allowing MODIS radiance to directly constrain the GEOS-Chem columnar mass of aerosols. Built upon this progress, *Wang et al*. [2012] further used MODIS radiance to constrain dust emissions over the East Asia.

[8] In this paper, we present a new attempt for the top-down estimate of aerosol emissions through integration of the satellite observation of reflectance and GEOS-Chem Adjoint model. The technique is applied to improve estimates of mineral dust and anthropogenic SO_2, NH_3, NO_x, black carbon (BC), and organic carbon (OC) emissions over China for April 2008, during which ground-based PM_{10} (particulate matter with aerodynamic diameter of 10 μm or less) data are available from a joint China-U.S. dust field experiment [*Huang et al*., 2010]. This paper differs from the past work in that: (a) satellite reflectance (in essence radiance) is used to constrain the emission estimates of aerosol particle and precursors, which eliminates the discrepancy of aerosol optical properties between model simulated and satellite retrieved AOD; (b) we use a suite of aerosol and gas measurements from satellite sensors and ground-based instruments to independently evaluate our results, and test our hypothesis that temporal variation of AOD at different locations, as characterized by satellite observations, can be a strong constraint for species-specific source estimates if they are combined with the model-based knowledge of the dominant aerosol sources and the source-receptor relationship at corresponding locations; and (c) combination of (a) and (b) will provide the basis and a necessary step forward for future research to simultaneously use both gas and AOD measurements to constrain speciated aerosol emissions.

[9] We describe the top-down inversion scheme and its key components (i.e., GEOS-Chem forward model and its adjoint, and observational constraints) in section 2. The top-down constraints on aerosol emissions over China for the period of April 2008 are presented in section 3, and evaluated in section 4. Interpretation and implications of the results are discussed in section 5, and section 6 summarizes this study.

2. Observational Constraints and Inversion Methodology

[10] As shown in Figure 1, the top-down inversion approach in this study integrates the MODIS radiance/reflectance with the GEOS-Chem (section 2.1) and its adjoint model (section 2.2) to optimize aerosol emissions. First, similar to *Wang et al*. [2010], we retrieve the atmospheric aerosol mass and AOD through fitting the calculated radiance based on GEOS-Chem aerosol composition and single optical properties to the MODIS cloud-free radiances (section 2.3). Second, the retrieved AOD (*hereafter retrieved MODIS AOD*) from the first step is used as an observational constraint to optimize the aerosol emissions by inverting the GEOS-Chem chemical transport model (section 2.4). The approach aims to improve aerosol emission estimates that ultimately will yield better agreement between model-simulated and satellite-observed reflectances. Since the aerosol single scattering properties are exactly the same between the retrieval algorithm and GEOS-Chem (as done in the first step), the top-down inversion scheme essentially uses the MODIS radiances (in the form of retrieved AOD) to scale the GEOS-Chem aerosol mass, which in turn are used to optimally adjust the aerosol emissions. The approach here is first demonstrated through a pseudo-observation experiment (section 2.5) before it is applied to real observations (section 3).

2.1. GEOS-Chem Model

[11] GEOS-Chem [*Bey et al*., 2001] (www.geos-chem.org) is a global three-dimensional tropospheric chemical transport model driven by assimilated meteorological observations from the Goddard Earth Observing System (GEOS) of the NASA Global Modeling and Assimilation Office. The aerosol simulation in GEOS-Chem includes state-of-science representations of the major aerosol components: sulfate (SO_4), nitrate (NO_3), ammonium (NH_4), BC, and OC in both hydrophilic and hydrophobic modes, mineral dust in four size bins, and sea salt aerosols in both accumulation and coarse modes. The model couples aerosol and gas-phase chemistry through nitrate and ammonium partitioning, sulfur chemistry, secondary organic aerosol formation, and uptake of acidic gases by sea salt and dust [*Park et al*., 2004]. Aerosol is removed by

dry and wet deposition. Dry deposition in GEOS-Chem follows a resistance-in-series scheme [*Wesely*, 1989; *Wang et al*., 1998] and accounts for gravitational settling [*Seinfeld and Pandis*, 1998] and turbulent mixing of particles to the surface [*Zhang et al*., 2001]. Aerosols are also removed through wet scavenging in convective updrafts as well as the first-order rainout and washout [*Liu et al*., 2001].

[12] GEOS-Chem uses many databases for anthropogenic emissions [*van Donkelaar et al*., 2008] and biomass burning emissions [*van der Werf et al*., 2010]. In the current study, the annually anthropogenic emissions of SO_2 and NO_x are from INTEX-B EI with the base year of 2006 [*Zhang et al*., 2009b]. The monthly anthropogenic and biofuel emissions of NH_3 use the TRACE-P EI with the base year of 2000 [*Streets et al*., 2003]. The monthly anthropogenic fossil fuel and biofuel OC/BC emissions are from Bond EI with base year of 2000 [*Bond et al*., 2007]. The monthly biomass burning emission for SO_2, NH_3, NO_x, OC, and BC use GFED2 EI with the base year of 2007 [*van der Werf et al*., 2010]. The mineral dust entrainment and deposition (DEAD) scheme [*Zender et al*., 2003] that was modified to combine with the GOCART topographic source function [*Ginoux et al*., 2001; *Fairlie et al*., 2007] is used to simulate the prior emitted dust fluxes (hereafter the modified DEAD scheme). We run version 8-02-01 of GEOS-Chem for the full chemistry simulation during the period of April 2008 with $2^\circ \times 2.5^\circ$ horizontal resolution and 47 vertical levels.

[13] AOD at wavelength λ in each layer is calculated from the sum of AODs of each component i assuming external mixing

$$\tau_\lambda = \sum_{i=1}^{n} \frac{3}{4} \frac{m_i\, Q_{\lambda,i}}{\rho_i\, r_{eff,i}} = \sum_{i=1}^{n} m_i\, \beta_{\lambda,i}$$

where n is the number of aerosol components, m_i is aerosol mass concentration of component i, $Q_{\lambda,i}$ is extinction efficiency factor at wavelength λ calculated with Mie theory, ρ_i is aerosol mass density, $r_{eff,i}$ is particle effective radius, and $\beta_{\lambda,i} = \frac{3}{4}\frac{Q_{\lambda,i}}{\rho_i\, r_{eff,i}}$ is the mass extinction efficiency. We account for the hygroscopicity of aerosol particles, as all parameters in the above equation are functions of relative humidity for hydrophilic aerosol components. We use the updated aerosol size distribution and refractive index from *Drury et al*. [2010] and *Wang et al*. [2010] to calculate $Q_{\lambda,i}$ and $r_{eff,i}$ in a Mie code.

2.2. GEOS-Chem Inverse Modeling

[14] The adjoint of the GEOS-Chem model was developed specifically for inverse modeling of aerosol (or their precursors) and gas emissions [*Henze et al*., 2007], and it is continuously improved and maintained by the GEOS-Chem Adjoint and Data Assimilation Working Group and its users (http://wiki.seas.harvard.edu/geos-chem/index.php/GEOS-Chem_Adjoint). The strength of the adjoint model is its ability to efficiently calculate model sensitivities with respect to large sets of model parameters, such as aerosol emissions at each grid box. These sensitivities can serve as the gradients needed for inverse modeling of aerosol emissions. Recent studies have used the GEOS-Chem adjoint with satellite observations to constrain sources of species such as CO, CH_4, and O_3 [*Kopacz et al*., 2009, 2010; *Jiang et al*., 2011; *Wecht et al*., 2012; *Parrington et al*., 2012], to diagnose source regions for long-range transport [*Zhang et al*., 2009a; *Kopacz et al*., 2011; *Henze et al*., 2009], and to provide guidance on future geostationary observations of surface air quality [*Zoogman et al*., 2011]. More recently, the adjoint for the GEOS-Chem dust emission and transport simulation has been developed and applied to optimize dust emissions from satellite observations over East Asia [*Wang et al*., 2012].

[15] In the GEOS-Chem inverse modeling framework, aerosol emissions are adjusted using a vector of control parameters $\boldsymbol{\sigma}$ that are the logarithm of emission scaling factors for aerosol emissions: $\boldsymbol{\sigma} = \ln(\mathbf{E}/\mathbf{E_a})$, where $\mathbf{E}$ and $\mathbf{E_a}$ are updated and prior aerosol emission vectors, respectively. The model response function J, or cost function, is formulated following the four-dimensional variational (4D-Var) technique:

$$J(\boldsymbol{\sigma}) = \frac{1}{2}\sum_{\mathbf{c}\in\Omega} [\mathbf{c}(\boldsymbol{\sigma}) - \mathbf{c}_{\text{obs}}]^T \mathbf{S}_{\text{obs}}^{-1} [\mathbf{c}(\boldsymbol{\sigma}) - \mathbf{c}_{\text{obs}}] + \gamma \frac{1}{2} [\boldsymbol{\sigma} - \boldsymbol{\sigma}_{\text{a}}]^T \mathbf{S}_{\text{a}}^{-1} [\boldsymbol{\sigma} - \boldsymbol{\sigma}_{\text{a}}]$$

where $\mathbf{c}$ is the vector of simulated aerosol concentration in four-dimensional spatial and temporal observation space $\boldsymbol{\Omega}$, $\mathbf{c}_{\text{obs}}$ is the vector of observed aerosol concentration, $\mathbf{S}_{\text{obs}}$ is the observation error covariance matrix for $\mathbf{c}_{\text{obs}}$, γ is a regularization parameter, $\boldsymbol{\sigma}_{\text{a}}$ is prior control parameters, and $\mathbf{S}_{\text{a}}$ is the error covariance matrix of $\boldsymbol{\sigma}_{\text{a}}$. Overall, the cost function is a measure of specific model response, the minimum value of which balances the objectives of minimizing model mismatch of the observations while ensuring the specified prior emissions remain within approximate range described by $\mathbf{S}_{\text{a}}$. The optimization seeks the optimal $\boldsymbol{\sigma}$ that minimizes the cost function J iteratively through a numerical quasi-Newton algorithm, the L-BFGS-B algorithm [*Byrd et al*., 1995], which requires the supplement of the cost function and its gradient with respect to the emission scaling factors calculated with GEOS-Chem adjoint model.

2.3. Observational Constraints from MODIS

[16] The observational constraints in this study are MODIS reflectances from both Terra and Aqua satellites, from which 4D mass concentrations of six aerosol species (namely, SO_4, NO_3, NH_4, BC, OC, and dust) have been derived with the GEOS-Chem model using the retrieval algorithm presented by *Wang et al*. [2010]. Key to this algorithm are: (a) a database of time-dependent local 0.65 and 2.1 μm surface reflectance ratio that are derived from samples of the MODIS dark-pixel reflectance data in low AOD conditions (i.e., dynamic lower envelope method), (b) an assumption that the simulated CTM aerosol is unbiased in composition and vertical distribution shape but possibly largely biased in total mass or optical depth, and (c) a linearized radiative transfer model (VLIDORT [*Spurr*, 2006]) that computes the top-of-atmosphere (TOA) reflectance and its Jacobian sensitivity to the column AOD using the GEOS-Chem single aerosol optical properties and the solar-earth-sensor geometries of the coincident MODIS scene. With above (a), (b), and (c), *Wang et al*. [2010] retrieved two unknowns (AOD at 0.65 μm and surface reflectance at 2.13 μm) from two MODIS observed quantities (0.65 and 2.13 μm TOA reflectance) by seeking the minimum differences between GEOS-Chem and MODIS reflectance. Based on (b), mass concentrations of individual aerosol species at each MODIS overpassed grid cell are updated by applying the AOD scaling factors (ratios of retrieved AOD to GEOS-Chem AOD at 0.65 μm) and are

Table 1. Prior, Posterior, and Perturbed Aerosol Emissions Over China in the Pseudo Experiment

Tracers	E_{prior} (Gg)	$E_{posterior}$ (Gg)	$E_{posterior}/E_{prior}$ (%)	$E_{perturbed}/E_{prior}$ (%)
SO_2	520.8	592.0	113.7	120
NH_3	219.3	249.2	113.7	120
NO_x	338.8	365.3	107.8	120
BC	23.3	23.8	102.3	100
OC	39.7	41.1	103.4	100
Dust	2310.3	1697.1	73.7	60

used as observational constraints for optimizing aerosol emissions. According to the evaluation of the retrieved AOD against AERONET AOD [*Wang et al*., 2010], we found the uncertainty is generally less than 20%, which we subsequently use to quantify the observation error in the inverse modeling optimization.

[17] GEOS-Chem-simulated aerosol composition over Asia is shown by multiple studies to have large underestimation in BC, and equivalent or larger underestimation of OC mass and overestimation of sulfate aerosol mass [*Heald et al*., 2005; *Fu et al*., 2012], which suggests that the mass fraction of highly absorbing (BC) and highly scattering (OC and sulfate) fine-mode aerosols may have far less biases (as compared to the relative bias in OC mass only). Consequently, no significant biases are assumed for: (a) the GEOS-Chem-simulated fraction of coarse-mode (dust) aerosol mass, and (b) the GEOS-Chem-simulated aerosol single scattering albedo. While (b) is important to ensure an unbiased retrieval of AOD, (a) supports that the GEOS-Chem-simulated dust AOD fraction is likely unbiased, both of which support the use of AOD scale factors derived from MODIS for constraining emission of coarse-mode dust and fine-mode aerosols. Admittedly, any model bias in modeled AOT fraction for each individual species can lead to a corresponding bias (of the same sign) in the adjoint modeling results for individual emission. Quantification of such bias is not possible for the present study owing to the lack of aerosol composition data in China.

2.4. Selection of Emissions for Optimization and Experiment Design

[18] The inversion scheme and the MODIS-based constraints, as described in the last three sections, are combined to constrain the aerosol emissions over the Eastern Asia for the period of April 2008. The modeled emission parameters that most significantly influence the discrepancy between simulation and observations are selected and spatially constrained. Specifically, those model parameters (or control parameters) represent six emitted tracers, as listed in Table 2, which include emissions of SO_2, NH_3, and NO_x, BC, and OC from anthropogenic sources, and mineral dust. Bottom-up inventories (and an online mobilization scheme for dust) are used as prior estimates, corresponding magnitudes and geographic distributions of which are shown in Table 2 and Figure 5, respectively. The temporal extent of the optimization window is selected to be reconcilable with the temporal variability of the bottom-up emission. We set optimization window of a month for those trace gases and carbonaceous emission tracers; while dust emission tracers are constrained daily in a separate optimization run following approach by *Wang et al*. [2012]. Both optimizations assimilate hourly observations during the adjoint simulation.

[19] The 4D-Var technique in the optimization requires background error covariance statistics for each control parameter. We specify the prior error for those emission tracers based on characterized spatial and temporal averaged uncertainties for those inventories [*Zhang et al*., 2009b; *Bond et al*., 2007; *Zender et al*., 2003] but with larger values to reflect the possibly large local aerosol emission uncertainties in the bottom-up inventories. The uncertainty for SO_2 emission estimate is believed to be smaller than those for NH_3 and NO_x, while uncertainties of other tracers could be even larger [*Textor et al*., 2006; *Zhang et al*., 2009b]. Therefore, we set relative error of 50% for SO_2, 100% for NH_3 and NO_x, 200% for BC, OC, and dust sources. Lacking information to fully construct a physically representative prior error covariance matrix, a regularization parameter γ is introduced in the cost function to balance the contribution of model error and source error, with a value (here $\gamma = 1000$) selected using the L-curve technique [*Hansen*, 1998]. Moreover, in order to test the impact of those specified uncertainties on the optimization, we run a case with an arbitrary prior error of 100% for all emission tracers and present the results in Table 3.

2.5. Sensitivity Test With AOD Pseudo-Observations

[20] We first conduct a pseudo experiment to assess: (a) the concept that temporal variations and geophysical location of AOD, when interpreted with GEOS-Chem model, can yield information about change regarding aerosol composition and emissions, and (b) the sensitivity of the inversion results to the assumption that GEOS-Chem-simulated relative composition or single scattering albedo of aerosol is unbiased. The experiment has three steps: (a) GEOS-Chem simulation with standard bottom-up EIs are first conducted to obtain prior aerosol composition and 0.65 μm AOD for the period from 5 to 11 April 2008; (b) Pseudo-observations of AOD are created by perturbing the following emissions (relative to bottom-up EIs) in GEOS-Chem: +20% for SO_2, NH_3, and NO_x, −40% for dust, and zero for BC and OC (Table 1); (c) These pseudo-observations of AOD in the dark surface region (red box in Figure 2a), twice per day, respectively, at the Terra and Aqua overpass daytime, are subsequently used as truth to constrain emissions using the GEOS-Chem adjoint-based inversion.

[21] The degree to which the inversion can correct for species-specific errors in the emissions is assessed in these sensitivity tests by comparing the optimized aerosol emissions with the perturbed emissions in (b). Figure 2 shows the distribution of relative changes in posterior emissions from the sixth iteration with respect to the prior bottom-up emissions for each species; the overall changes over the China are shown in Table 1. By the sixth iteration, the cost function reduced by 50%; further iterations yielded negligible additional decreases. The posterior emissions for SO_2 and NH_3, which increased by 14% from the prior, are close to the "truth" (20%). NO_x emissions were increased by 8%, a smaller change than SO_2 and NH_3. Dust emissions reduced by 26% in the inversion, approaching the true values of −40%. BC and OC emissions were increased by 2 and 3%, which are close to the truth of 0%.

[22] Overall, this sensitivity study demonstrates that the inversion is capable of resolving the sign, spatial distribution,

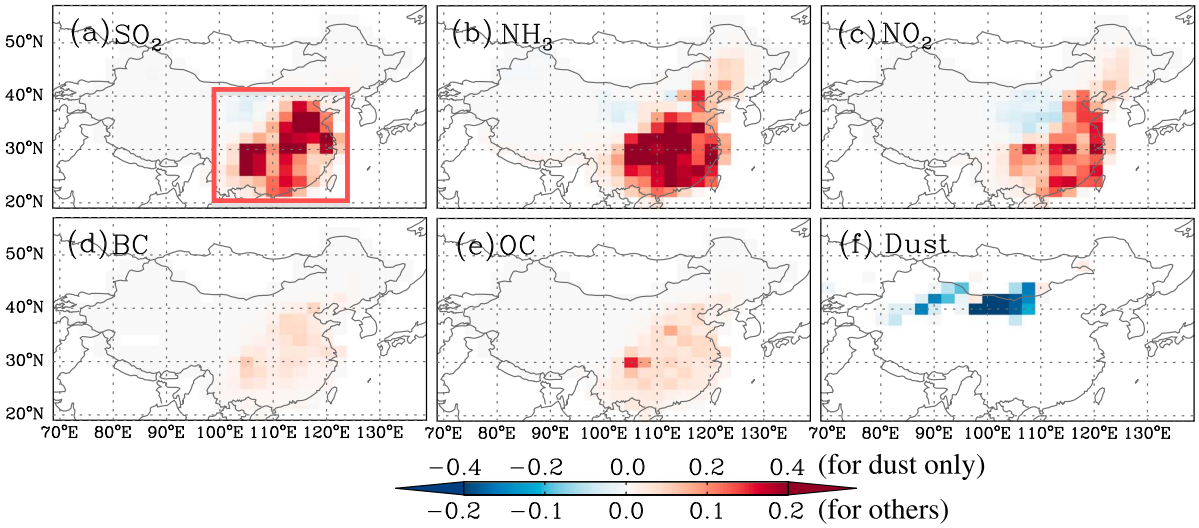

Figure 2. Relative changes in posterior aerosol emissions from a priori in the pseudo-observation experiment. Six panels are, respectively, for anthropogenic emissions of SO_2, NH_3, NO_x, BC, and OC, and mineral dust from both natural and anthropogenic sources. The red box in Figure 2a indicates the region where AOD observations are selected.

and the bulk of the true perturbations for the emissions of each species. Meanwhile, we also note that the adjoint inversion could transfer (somewhat marginal) errors from one tracer to another, such as increases in BC and OC emission as a result of significant underestimations in the prior SO_2, NH_3, and NO_x emissions, reflecting errors due to assumptions related to unbiased GEOS-Chem aerosol composition. We can also assume that similar aliasing would occur in attempts to distinguish the impacts of colocated precursor emissions of scattering particles (e.g., SO_2 and NO_x from power plants), although additional tests would be necessary to assess whether or not differences in the timescales (and thus transported length scales) over which these emissions impact AOD would allow their sources to be separated. Long-range transport of dust appears to have less influence on the inversion because: (a) except dust, there are little (other) emissions in dust source regions; (b) a sudden increase of AOD in downwind regions can be interpreted by

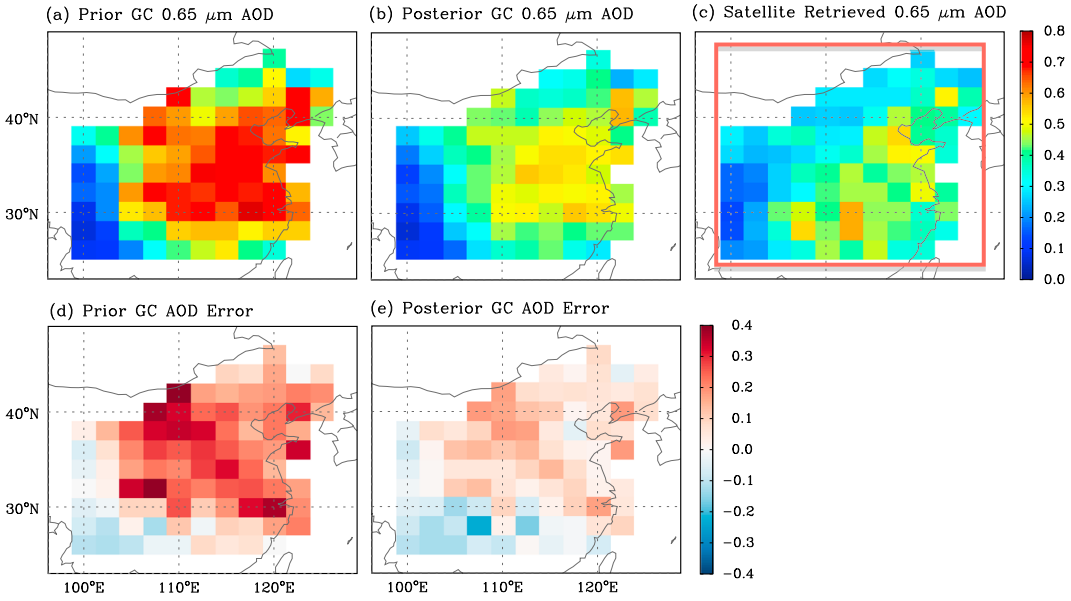

Figure 3. Comparison of the (a) prior and (b) posterior GEOS-Chem (GC) simulation of 0.65 μm AOD with the AOD at the same wavelength retrieved from MODIS reflectance using GEOS-Chem aerosol optical properties (c) averaged for the period of April 2008. Satellite retrievals with 10 km × 10 km at nadir are aggregated to GEOS-Chem grid cells; and the model AOD are sampled coincidentally with those retrievals. Figure 3d and 3e, respectively, show the difference of prior and posterior simulated from the satellite retrieved AODs. The red box in Figure 3c indicates the region where AOD observations are selected.

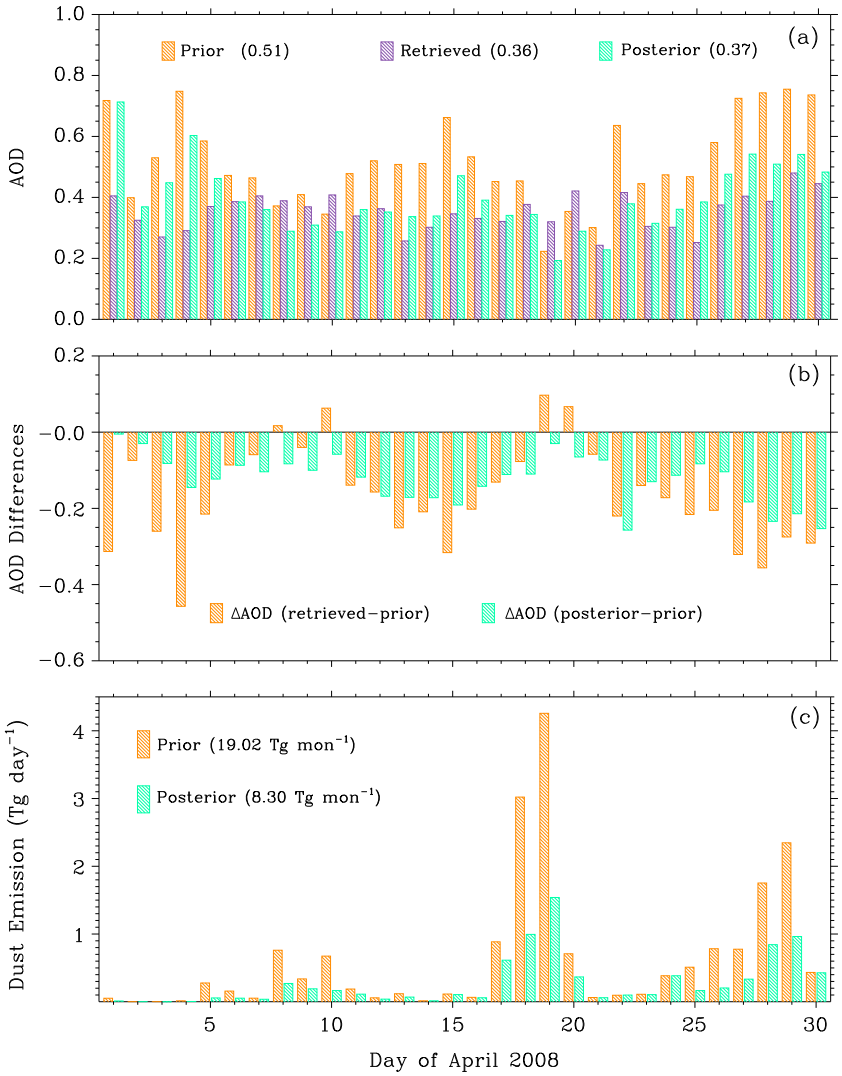

Figure 4. (a) Time series of the spatially averaged daily MODIS AOD retrievals (purple) for April 2008 over the Eastern China, compared by the prior (orange) and posterior (green) spatial averaged daily GEOS-Chem AOD that are sampled in the MODIS AOD tempo-spatial space. (b) Time series of the expected daily AOD adjustments (orange) that are the differences between MODIS AOD and the prior GEOS-Chem AOD and their real adjustments (green) that are the differences of posterior from prior GEOS-Chem AOD. (c) Time series of the prior (orange) and posterior (green) daily dust emissions over China for April 2008.

GEOS-Chem due to the dust transport, and this increase can be used by GEOS-Chem adjoint as constraint to optimize the dust emission.

3. Inversion Results

[23] With the feasibility of the approach demonstrated in section 2, we apply the approach to MODIS radiance data in April 2008. The emissions that result from each iteration during the optimization enable GEOS-Chem to produce a different set of AOD values that converge to the observational constraints. Figure 3a shows the geographic distribution of GEOS-Chem AOD at 0.65 μm, simulated with prior aerosol emissions, averaged coincidently with retrieved daily MODIS AOD (Figure 3c) during April 2008. While the prior model simulation captures the overall spatial pattern of AOD with larger values over eastern China, it has a slight underestimation over the southwestern China but an overwhelming overestimation elsewhere, when compared to the retrieved AOD from MODIS radiance (Figure 3d). The optimization is expected to adjust aerosol emissions to reduce those differences. Following the experiment design described in section 2.4, we find that after six iterations of the GEOS-Chem forward and adjoint runs, the cost function is reduced by about 60%, and further iterations yield negligible reductions in the cost function. Therefore, the aerosol emissions adjusted in iteration 6 are selected as the final optimal results. As shown in Figures 3b and 3e, the posterior GEOS-Chem AOD that are simulated with the optimized aerosol emissions are in much better agreement with their counterparts retrieved from MODIS reflectance, which is also reflected by the cost function reduction and confirms the effectiveness of the adjustment in top-down emissions.

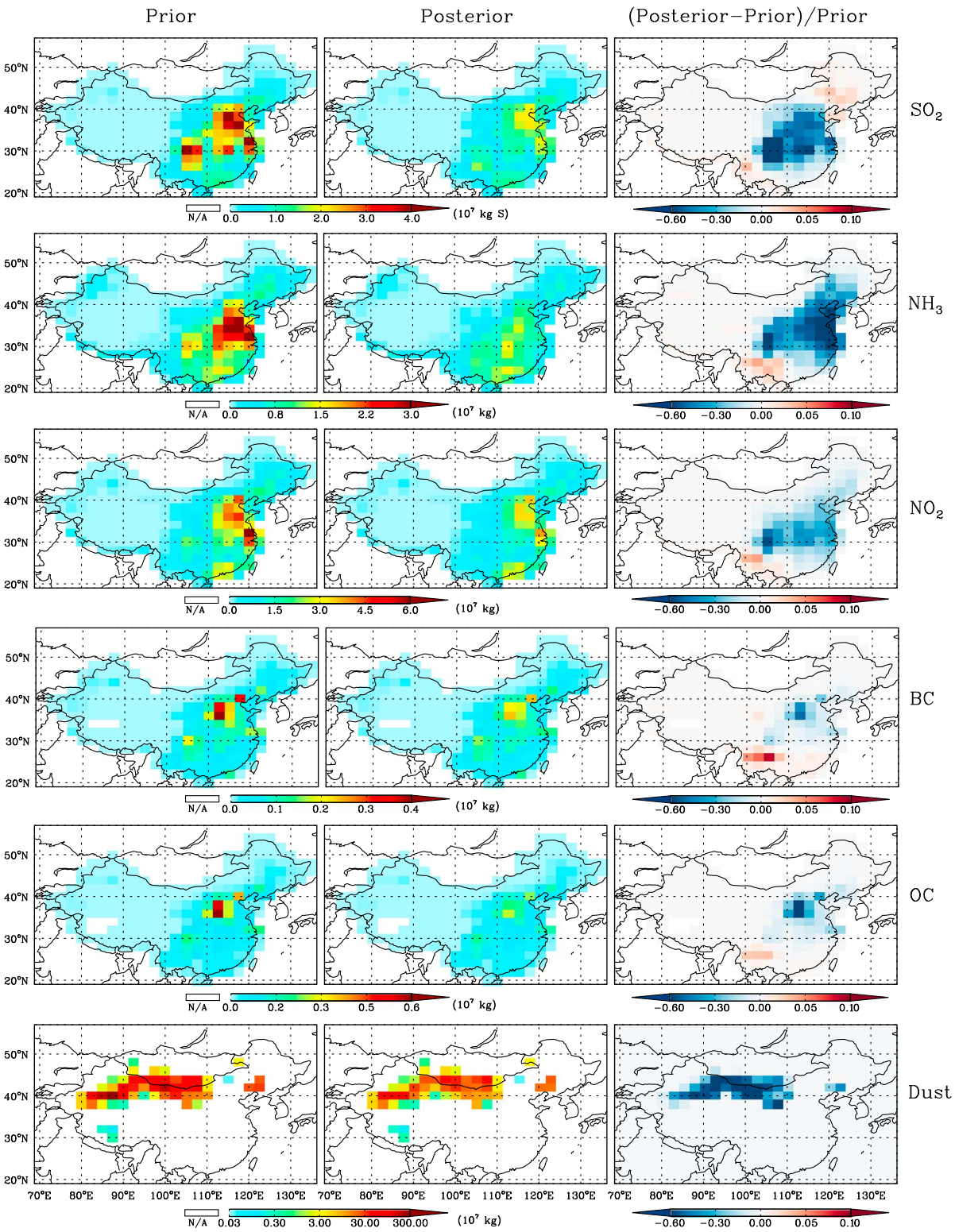

Figure 5. The prior (or bottom-up based, left column), optimized (or top-down constrained, middle column) aerosol emissions over China for the period of April 2008, and their relative differences (right column). Six rows from top to bottom are, respectively, for anthropogenic emissions of SO_2, NH_3, NO_x, BC, and OC, and mineral dust from both natural and anthropogenic sources.

[24] The convergence of the model simulation to the MODIS AOD retrievals is also indicated in the AOD daily variability. Figure 4a shows the daily variations of the AOD spatially averaged for available MODIS retrievals (purple) over the eastern China areas within the red box in Figure 3c, and the coincidental GEOS-Chem simulation prior and posterior to the aerosol emission optimization (orange and green, receptively). The prior model produces overestimated

Table 2. List of Prior and Posterior Aerosol Emissions in China During April 2008

	Bottom-Up					Top-Down		
Tracer	E_{prior} (Tg mon^{-1})	A Priori Error (%)	Base Year	Temporal Variability	Inventory	Optimizing Window	$E_{posterior}$ (Tg mon^{-1})	ΔE (%)
SO_2	2.60	50	2006	Annual	INTEX-B	1 month	1.73	−33.5
NH_3	1.10	100	2000	Annual	INTEX-B	1 month	0.72	−34.5
NO_x	1.69	100	2006	Monthly	INTEX-B	1 month	1.38	−18.8
BC	0.11	200	2000	Monthly	Bond-2007	1 month	0.10	−9.1
OC	0.21	200	2000	Monthly	Bond-2007	1 month	0.18	−15.0
Dust	19.02	200	Online	1 hour	DEAD	1 day	8.30	−56.4

AODs for most days during the month. After top-down adjustments to the aerosol emissions, such overestimation of the AOD is reduced in total over the course of the month. As shown in Figure 4b, the real changes of the modeled daily AOD during the optimization (green bars), or equivalently, the differences of the posterior from the prior are consistent with the expected changes, i.e., the differences of the MODIS retrievals from the prior model simulation. It is noted that the posterior AODs have larger departure from the observation than the prior on a few days. This reflects that monthly scaled emissions are not perfectly capturing the daily variation of emission.

[25] Emissions of SO_2, NH_3, NO_x, BC, and OC from anthropogenic sources are optimized monthly and rescaled over each individual 2° by 2.5° grid cell of China for the month of April 2008. The prior and posterior (optimized) emissions of those tracers are, respectively, shown in left and middle columns of Figure 5, in which the relative changes of those emissions in the optimization are also included in the right column. Overall, the optimization yields an overwhelming reduction for all emission tracers, even though some local increases are found. As expected, such adjustment in the constrained aerosol emissions is consistent with the changes in GEOS-Chem AOD before and after optimization, as aerosol loadings usually positively respond to the aerosol emissions. Quantitatively, anthropogenic emissions over China continent for the study period are changed by −33.5% for SO_2 from 1.302 to 0.866 Tg, −34.5% for NH_3 from 1.096 to 0.718 Tg, −18.8% for NO_x from 1.694 to 1.375 Tg, −9.1% for BC from 0.11 to 0.10 Tg, and −15.0% for OC from 0.205 to 0.175 Tg (Table 2). The largest reduction occurs sharply in the central regions of the Eastern China, corresponding to the region where the largest AOD are adjusted to the MODIS retrievals. Small increases of emitted anthropogenic sources of gases and carbonaceous particles are found over the southwestern China, which can be explained as the response for the underestimation of AOD in the model simulation over these regions (Figures 3a and 3d).

[26] The mineral dust emissions from both anthropogenic and natural sources are optimized daily. The adjoint has no leverage to increase the dust emissions over grid cells having zero dust emission in the prior estimate identified by the modified DEAD scheme. Thus, the posteriori dust source region remains unshifted as shown in Figure 5 (bottom panels), which is reasonable because the expansion or shrinkage of desert regions is unlikely to extend beyond the grid size (2° × 2.5°) of this study [*Zender et al*., 2003; *Fairlie et al*., 2007]. The total amount of the optimized dust emissions for April 2008 over China is 8.3 Tg, reduced by 56.4% from the modified DEAD module simulation of 19.02 Tg. Such reduction indicates an overestimation in the prior emissions of dust, especially over Gobi deserts that are located in the Northwestern China and the southern Mongolia. *Wang et al*. [2012] presented a similar result, but only for a dust event that occurred in the later portion of our study time period. Figure 4c illustrates the time series of the prior and optimized daily total dust emission. Two sharp peaks of the dust emissions indicate the occurrences of strong dust storms after April 15. Such large temporal variation in the daily scale requires the optimization of dust emission on the daily basis.

[27] An additional case with specified error of 100% for all the anthropogenic emission tracers is conducted to examine the sensitivity of those specified error to the optimization. Table 3 shows the relative change in optimized emissions for two different scenarios. Less than 0.5% difference in the optimized emissions is found, which means the uncertainty in prior emission could have much smaller impact on the optimization than the observational constraints.

4. Results Evaluations with Independent Measurements

[28] Because direct measurements of the aerosol emissions are few over China, we assess the optimized sources by comparing the GEOS-Chem posterior-simulated aerosol mass concentrations and AOD with the independent observations from various sources. The evaluation datasets include: (a) AERONET AOD observations [*Holben et al*., 1998] over nine sites; (b) Level 3 Multi-angle Imaging SpectroRadiometer (MISR) daily AOD products [*Kahn et al*., 2005]; (c) Level 3 SO_2 [*Krotkov et al*., 2006; *Lee et al*., 2009] and Level 2 NO_2 [*Bucsela et al*., 2006] retrievals from the OMI; (d) surface mass concentration of sulfate-nitrate-ammonium (SNA) aerosol particles over Qingdao, China; and (e) surface PM_{10} over two sites close to dust source region [*Ge et al*., 2010].

Table 3. Test of the Sensitivity of Optimization With Respect to Prescribed A Priori Error

	Case 1		Case 2	
Tracer	A Priori Error (%)	ΔE (%)	A Priori Error (%)	ΔE (%)
SO_2	50	−33.5	100	−33.7
NH_3	100	−34.5	100	−34.4
NO_x	100	−18.8	100	−18.8
BC	200	−9.1	100	−9.1
OC	200	−15.0	100	−15.0

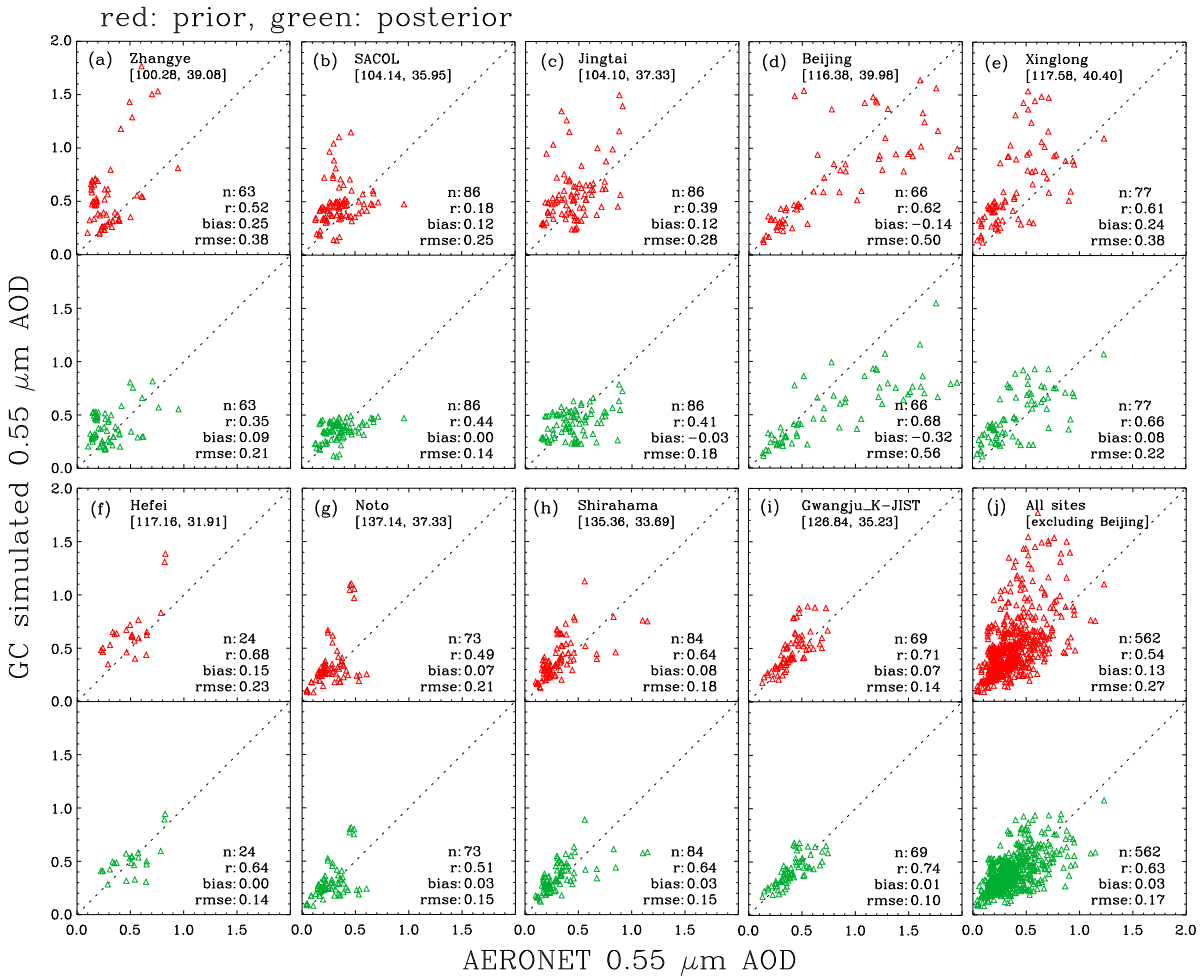

Figure 6. (a – i) Scatterplots of GEOS-Chem AOD versus AERONET AOD at 0.55 μm prior (red scatters) and posterior (green scatters) to the aerosol emission optimization over nine stations. AERONET AODs are 3 h averages following the GEOS-Chem output frequency. (j) The overall comparison for eight AERONET sites excluding Beijing. Also shown are the number of valid sampled pairs (n), correlation coefficients (R), bias, and root-mean-square-error (RMSE).

4.1. Comparison With AERONET AOD

[29] We first evaluate the prior and posteriori GEOS-Chem 0.55 μm AOD against the AERONET AOD at 0.55 μm that are interpolated from AODs at 0.44 and 0.67 μm based on the Angstrom exponent. Three-hour averaged values of available AERONET AOD, centered by the model output time, are used to compare with the model AOD over the grid cells locating the AERONET sites. The scatterplots shown in Figure 6 are the comparisons for nine stations over China, South Korea, and Japan representing different aerosol types. The first three stations, i.e., (a) Zhangye, (b) SACOL, and (c) Jingtai, which are located over rural regions in the south boundary of Gobi deserts and have little influence from anthropogenic emissions, are representative sites for dust aerosol [*Ge et al.*, 2010]. The next three sites, (d) Beijing, (e) Xinglong, and (f) Heifei, are located in anthropogenic source regions. The last three sites, (g) Noto, (h) Shirahama, and (i) Gwangju_K, are located over Japan and South Korea, the downwind regions of China emissions. Those last six stations are affected not only by the local anthropogenic emissions but also by the long-range transported aerosols from the upwind regions. Indeed, those three categories of stations are, respectively, located in the upwind, central, and downwind of regions having the observational constraints.

[30] The prior GEOS-Chem simulation (shown in the red scatter panels) overestimates the AERONET AOD for all the sites except Beijing. The low bias of model AOD at Beijing is likely owing to the model coarse resolution, which fails to resolve heavy local urban pollution. The geographic area of urban Beijing is about 1300 km^2 (http://en.wikipedia.org/wiki/Beijing), less than 3% of the area of a GEOS-Chem grid cell. Thus, the local pollution signal is smeared in the model grid box. Moreover, Beijing and Xinglong are in the same model grid cell, but AERONET AOD over Xinglong is much smaller than that over Beijing site (as later shown as circles on the maps of Figures 7a–c). As Beijing site is difficult to represent in the GEOS-Chem at $2^\circ \times 2.5^\circ$ resolution, we exclude Beijing site in our further analysis. GEOS-Chem AOD from the posterior aerosol emissions are in more agreement with the AERONET AOD (shown in the green scatter panels), as indicated by reduced bias and root-mean-square-error

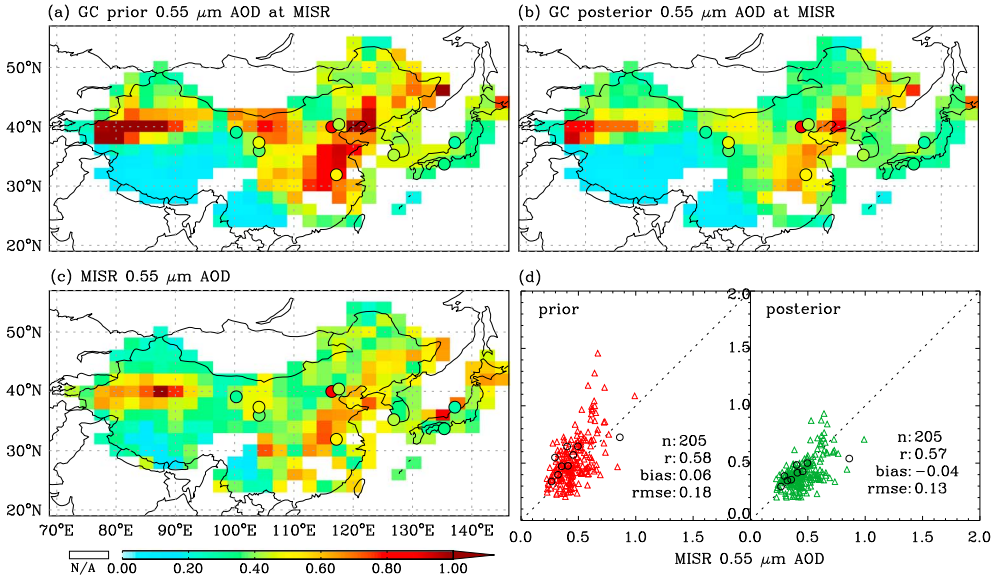

Figure 7. Comparison of the prior and posterior GEOS-Chem simulation of 0.55 μm AOD with the Level 3 MISR 0.55 μm AOD for the period April 2008. (a) The prior GEOS-Chem 0.55 μm AOD that are sampled coincidentally with MISR AODs for the period of April 2008. Also overlaid circles are the monthly AOD averages at 0.55 μm observed from the nine AEORNET sites shown in Figure 5. Figure 7(b) Same as Figure 7a but for the monthly average of posterior GEOS-Chem AOD. (c) Monthly average of the Level 3 daily MISR 0.55 μm AOD. (d) Scatterplot of the GEOS-Chem AOD versus the MISR AOD before (red scatters) and after optimization (green scatters), in which each point indicates an AOD pair over a model grid cell with value over 0.2. Also shown are the statistics including number of sampled pairs (n), correlation coefficient (R), bias and root-mean-square-error (RMSE). Comparisons of the monthly GEOS-Chem AOD versus AERONET AOD are also included as the black circles; each circle indicates an AOD pair over an individual site.

(RMSE) over all the other sites and increased correlation coefficients (R) for most sites. The overall comparison (Figure 6j) shows the correlation coefficient increases from 0.54 to 0.63, and the bias (RMSE) declines from 0.13 (0.27) to 0.03 (0.07).

4.2. Comparison With MISR AOD

[31] We regrid the Level 3 daily MISR 0.55 μm AOD from the $0.5° \times 0.5°$ resolution to GEOS-Chem $2° \times 2.5°$ grid cells and take monthly average for April 2008, the geographic distribution of which is shown in Figure 7c. High AOD values are found over the eastern China and the northwestern desert regions, which are associated to the anthropogenic pollution primarily from the industry and wind-blown mineral dust, respectively. The monthly sun-photometer AOD values at the same wavelength show good agreements with the MISR AOD over all the AERONET sites except Beijing where the significant local urban pollution exists.

[32] The monthly averages of prior and posterior GEOS-Chem 0.55 μm AOD mapped in Figures 7a–b are sampled coincidently to the MISR AOD. A comparison with the MISR AOD shows GEOS-Chem simulation with prior aerosol emissions overestimates AOD over both the desert and industrial regions. The posterior simulation is slightly more in agreement with MISR AOD. To facilitate the comparison of model with MISR AOD, we also include, as Figure 7d, the scatterplots of the AOD for each GEOS-Chem grid cell with values larger than 0.2 by considering the larger retrieval uncertainty in the low AOD conditions [*Kahn et al.*, 2005]. While the correlation coefficients remain about the same, both absolute bias and RMSE are reduced about 30%.

4.3. Comparisons With OMI Column SO_2 and NO_2

[33] The improvement in the optimized aerosol emissions is also exhibited in the comparison of simulated trace gases to the satellite retrievals from OMI. The GEOS-Chem SO_2 simulations are assessed with OMI Level 3 daily products of planetary boundary layer (PBL) SO_2 column gridded with $0.25° \times 0.25°$ resolution. We average the OMI SO_2 column retrievals into GEOS-Chem $2° \times 2.5°$ grid cells and take the monthly average for comparison, which are shown in Figure 8c. Figures 8a and 7b show model prior and posterior SO_2 column that are coincidentally sampled with OMI retrievals. Figure 8d illustrates the quantitative analysis for OMI SO_2 retrievals larger than 1×10^{16} molec cm^{-2}. With the optimized emission estimates, the bias and RMSE are reduced from 0.81 and 0.61 to –0.28 and 0.38 molec cm^{-2}, respectively, along with an increase of correlation coefficient from 0.68 to 0.73.

[34] We evaluate the model simulation of NO_2 with OMI Level 2 products of NO_2 tropospheric column over $0.25° \times 0.25°$ grid cells. Recent studies suggested that the uncertainty in OMI NO_2 tropospheric column retrievals is ~40% with an ~15% positive systematical bias [*Boersma et al.*, 2008; *Celarier et al.*, 2008]. Following *Lin et al.* [2010], we apply a factor of 0.85 to OMI NO_2 retrievals in our comparison to correct the bias. Figure 9 shows the comparison of GEOS-Chem NO_2 columns with

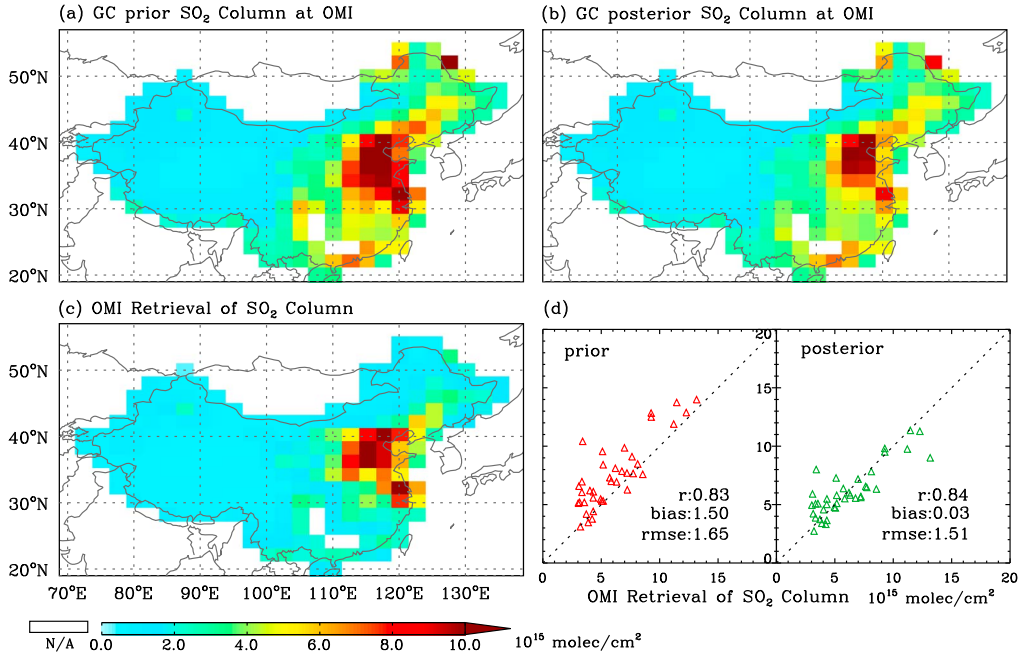

Figure 8. Same as Figure 7 but for comparison of the GEOS-Chem SO_2 simulation with OMI column SO_2 retrievals for the period of April 2008. The OMI planetary boundary layer (PBL) column SO_2 from the Level 3 daily products with $0.25° \times 0.25°$ resolutions are aggregated into GEOS-Chem grid cells.

regridded OMI NO_2 retrievals. Similarly, we also perform the quantitative analysis, as in Figure 9d, for OMI NO_2 column retrievals larger than 3.0×10^{15} molec cm^{-2}. While the correlation coefficient remains about the same, the bias (RMSE) is reduced from 1.50 (1.65) to 0.03 (1.51) (units: 10^{15} molec cm^{-2}) after constraining aerosol emissions.

4.4. Comparisons With Near-Surface Aerosol Mass Concentrations

[35] The accuracy of the SNA aerosol simulation is in part determined by the representation of the emissions of SO_2 and NO_x and NH_3, and hence GEOS-Chem simulations with constrained emissions should provide overall an improved simulation of SNA. Figure 10 shows the comparison of daily

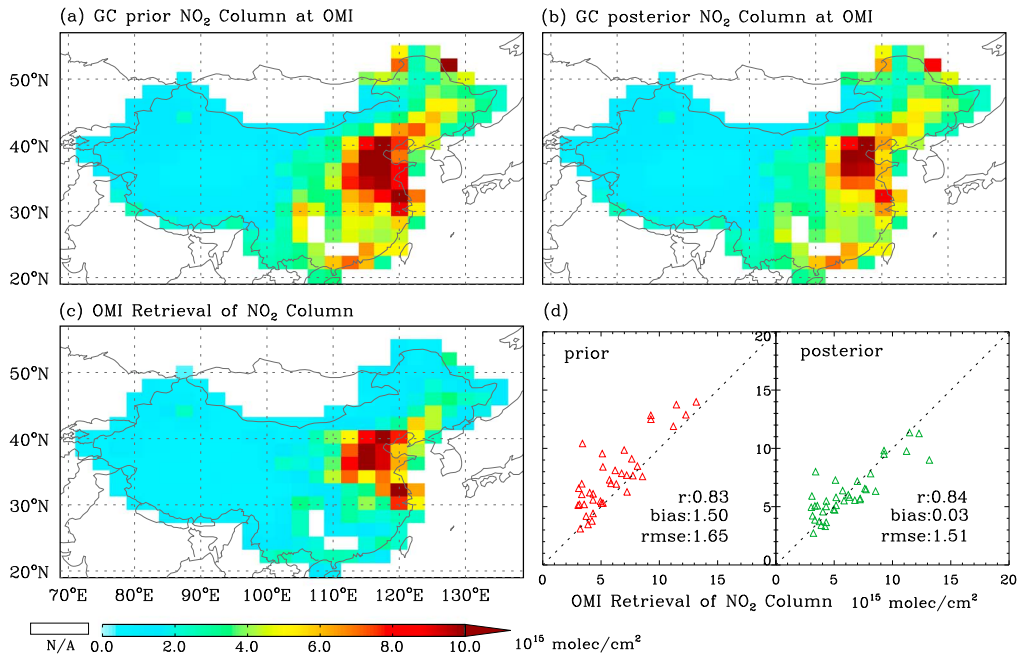

Figure 9. Same as Figure 7 but for comparison of the GEOS-Chem NO_2 simulation with OMI column NO_2 retrievals for the period of April 2008. The OMI tropospheric column NO_2 from Level 2 daily products with $0.25° \times 0.25°$ resolutions are aggregated into GEOS-Chem grid cells.

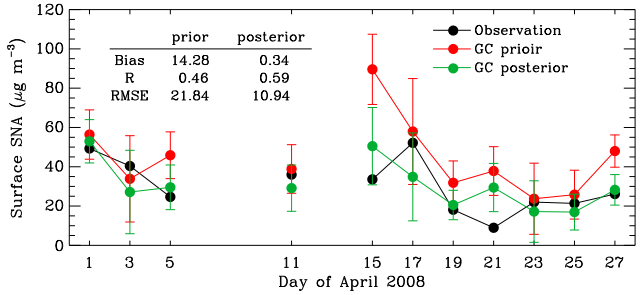

Figure 10. Comparison of the GEOS-Chem surface mass concentration of sulfate-nitrate-ammonium (SNA) aerosols with ground-based observations over Qingdao (120.34°E, 36.06°N), China. Discontinuity in time series is due to missing or quality filtered observations. Circles indicate the change of AOD values observed by AERONET stations.

near-surface SNA mass concentration from the prior and posterior GEOS-Chem simulations with measurements over Qingdao (120.34°E, 36.06°N), China. The error bars for the GEOS-Chem curves indicate the diurnal standard deviation. An overestimation in the prior model surface SNA simulations is found when comparing with observed counterparts, which shows a bias of 14.28 μg m^{-3}, RMSE of 21.84 μg m^{-3}, and correlation coefficient of 0.46. Such bias is significantly reduced to 0.34 μg m^{-3} in the simulation with top-down constrained emissions, along with a 50% decrease in RMSE and a 28% increase in correlation coefficient.

[36] The mass concentration over or near the dust source regions where the anthropogenic emissions are small is most sensitive to the dust mass loading, and thus can be an indicator of the dust emissions in the first order. Figure 11

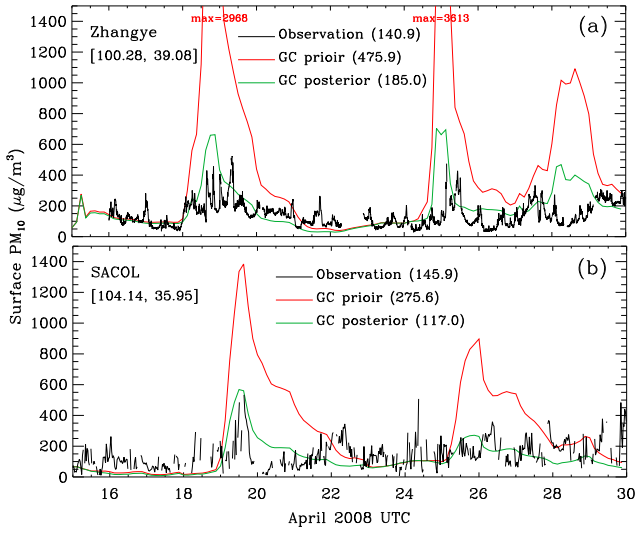

Figure 11. Time serial plot of the GEOS-Chem-simulated surface PM10 concentrations by prior (red) and posterior (red) aerosol emissions compared with the in situ measured PM10 (black) over (a) Zhangye and (b) SACOL stations for 15 – 30 April 2008; also shown are the average values over same the period. Discontinuity in time series is due to missing or quality filtered observations.

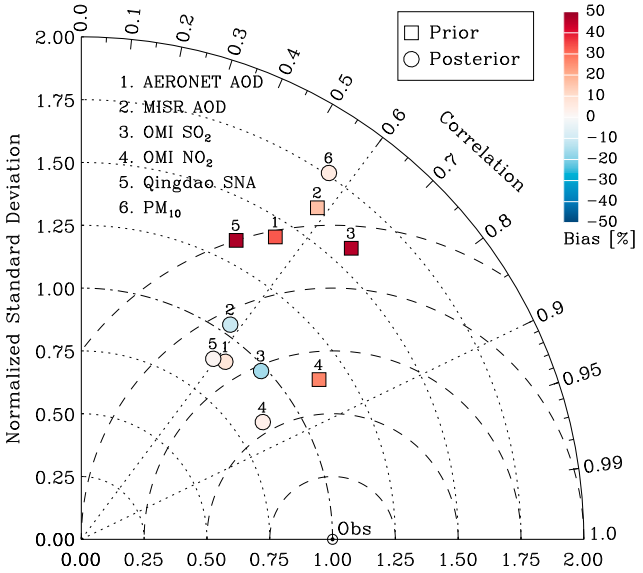

Figure 12. Taylor diagram for the model evaluations before (squares) and after (circles) optimization when comparing against (1) AERONET AOD at 0.55 μm, (2) MISR 0.55 μm AOD, (3) OMI column SO2, (4) OMI column NO2, (5) surface SNA concentrations at Qingdao site, and (6) surface PM_{10} concentrations measured at Zhangye and SACOL sites. The color coded on each point indicates the relative bias. It should be noted that the ratio of standard deviations and correlation coefficient between prior GEOS-Chem-simulated and measured surface PM_{10} over Zhangye and SACOL is 6.5 and 0.45, which makes the point number 6 for the prior simulation far beyond the range of this Taylor diagram.

shows the prior and posterior GEOS-Chem surface PM_{10} mass concentration compared with the ground-based measurements from the 2008 China-U.S. joint field experiment [*Ge et al.*, 2010] over two of the AERONET sites in Figures 6a and 6b, i.e., Zhangye (100.28°E, 39.08°N) and SACOL (204.14°E, 35.95°N), which are located on the downwind boundaries of the Gobi deserts. Based on the availability of the measurements data, comparisons are for the period of 15 – 30 April 2008. The measured surface PM_{10} shows a strong daily variation. A strong dust event during 18 – 20 April can be found over both stations with PM_{10} exceeding 400 μg m^{-3}. Two additional dust events with PM_{10} over 400 μg m^{-3} occurred during 24 – 26 and 29 – 30 April. The prior simulation generally captures the daily variation pattern but significantly overestimates the surface PM_{10} for those dust events; prior simulated PM_{10} reaches up to around 3000 μg m^{-3} over Zhangye and 1000 μg m^{-3} over SACOL for the dust events during 18 – 20 and 24 – 26 April 2008. The two-week averages show the prior simulation overestimates PM_{10} a factor of 2 over Zhangye and a factor of 1 over SACOL in the magnitude. After optimization, the relative biases in the PM_{10} simulation are reduced to about 25%. Moreover, the comparison of the time series of the PM_{10} also shows that the model value with top-down emissions has much better agreement with the measurements in terms of temporal variation.

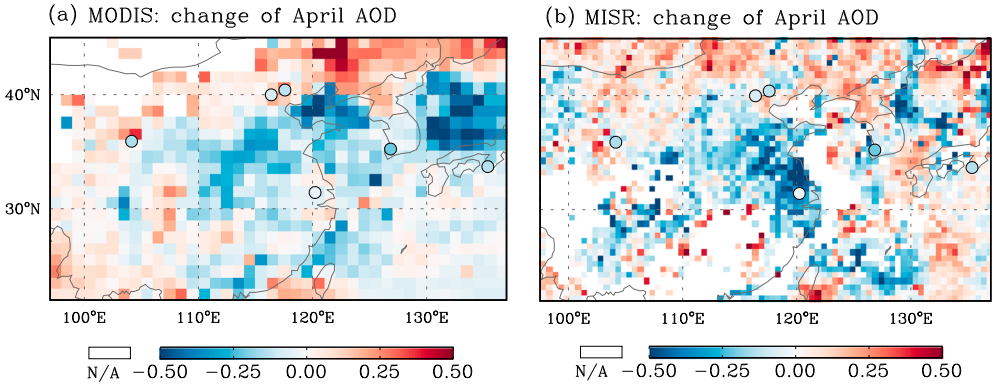

Figure 13. Change of April monthly 0.55 μm AOD from 2006 to 2008 from (a) MODIS and (b) MISR Level 3 daily products.

4.5. Evaluation Summary

[37] A summary of evaluations of the prior and posterior model simulations is illustrated in Figure 12 using a Taylor diagram [*Taylor*, 2001]. Taylor diagram provides a statistical summary of the model performance in terms of correlation coefficients (R), centralized root-mean-square difference (RMSD), and ratio of standard deviations between model and observations (or normalized standard deviation, NSD). The latter two quantities reflect how well model captures the temporal or/and spatial variation of observations. In the Taylor diagram, cosine of polar angles represents R, and radius (dotted-contour) indicates NSD. Thus, the reference point (black circle) where R and NSD are unity represents observations, and the distance (dashed-contour) of certain point from which indicates the RMSD. Considering that the Taylor diagram itself is not able to show the statistical bias, we use different colors for each data point to indicate their respective relative biases. The data points labeled from 1 to 6 indicate comparisons between model and observations of (a) AERONET AOD at 0.55 μm, (b) MISR 0.55 μm AOD, (c) OMI retrievals of SO_2 Column, (d) OMI retrievals of NO_2 Column, (e) surface concentration of SNA over Qingdao, and (f) surface concentration of PM_{10} over Zhangye and SACOL, respectively. Square and circles represent the evaluations for prior and posterior GEOS-Chem simulations, respectively. It should be noted that the NSD between prior GEOS-Chem-simulated and measured surface PM_{10} during the China-U.S. joint field campaign is about 6.5 (and R of 0.45) that are significantly beyond the range of this Taylor diagram. Consequently, the square point of number 6 is not shown in the diagram. It is clear from the Taylor diagram that the circular points (posterior simulation) are generally closer than the square points (prior simulation) to the reference point and to the unity curve of NSD, and have remarkably decreased bias. Evaluations with all those independent observations indicate a notable improvement in the model simulation, reflecting a better estimate of aerosol emissions.

Table 4. Comparisons for Annually (Tg yr^{-1}) and/or for April Only (Tg mon^{-1}) Estimates of Chinese Aerosol Emissions During 2006 and 2008

		2006		2008	
Trace	Inventories	Annual	April	Annual	April
SO_2	INTEX-B, *Zhang et al.* 2009b	31.02	2.37		
	China MEP-2008	25.89		23.21	
	Lu et al. 2010	33.2		31.3	
	This work		2.60	22.69[a]	1.73
NH_3	TRACE-P, *Streets et al.* 2003	13.6	1.10		
	Huang et al. 2012	9.8	0.71		
	This work		1.10	8.91[a]	0.72
NO_x	INTEX-B, *Zhang et al.* 2009b	20.83	1.63		
	Lin et al. 2010			22.34	
	This work		1.69	17.60	1.38
BC	INTEX-B, *Zhang et al.* 2009b	1.81	0.12		
	Qin and Xie, 2012	1.55		1.61	
	Lu et al. 2011	1.63		1.68	
	Zhao et al. 2013	1.6		1.6	
	This work		0.11	1.51[a]	0.10
OC	INTEX-B, *Zhang et al.* 2009b	3.22	0.19		
	Lu et al. 2011	3.42		3.37	
	Zhao et al. 2013	2.9		2.8	
	This work		0.21	2.92[a]	0.18

[a]Annual top-down estimates (Tg yr^{-1}) based on the monthly variation of the INTEXT-B inventory.

5. Implication of Results

[38] Interpretation of our inversion results can be from two different perspectives. First, if assuming that bottom-up anthropogenic emissions are the best estimates for their base years (mostly 2006), the reduction in the top-down emissions over China for April 2008 may indicate a decrease of emissions for April from 2006 to 2008. This conjecture is supported by the finding of significant decrease of AOD from 2006 to 2008 over the eastern China, shown both in the MODIS and MISR Level 3 gridded products (Figure 13), if we assume that the impact on AOD of meteorological differences between the two years is smaller than the differences in emissions. Furthermore, a slight increase of AOD over the Southeastern China (Figure 13) is also found to be consistent to the increase in the top-down emission estimates (Figure 5). In contrast to the first interpretation, the second one is that the difference of actual emissions between 2008 and their base year (2006) is smaller than the magnitude of adjustments in the optimization, and hence our results imply that the prior bottom-up emissions might be artificially overestimated. We further elucidate those two points below with a literature survey (data are summarized in Table 4).

5.1. SO_2

[39] The INTEX-B inventory by *Zhang et al*. [2009b] reported an annual production of 31.02 Tg from anthropogenic sources over China. A decrease trend of China SO_2 emissions from 2006 to 2008 has been found based on bottom-up estimates by *Lu et al*. [2010] from 33.2 to 31.3 (~5.8% decrease) Tg yr^{-1} and by China *Ministry of Environmental Protection* [2009] (hereafter referred to as MEP-2008) from 25.9 to 23.2 Tg yr^{-1} (~10.4% decrease). With OMI SO_2 retrievals, *Lu et al*. [2010] found the dramatic reduction of SO_2 emissions over the northern China for the same period. Similar to this study, *Lu et al*. [2010] also presented that the reductions are more significant over the Eastern China. They attribute some reduction to the widespread installation of flue-gas desulfurization devices in power plants, which is enforced by the China government since 2006. Evidences for the reduction trend of SO_2 emission also include the reduction of SO_2 column from 2006 observed by both SCIAMACHY and OMI satellite sensors [*Lu et al*., 2011]. With the same SCIAMACHY and OMI SO_2 retrievals, *Lee et al*. [2011] obtained top-down estimates of China SO_2 emissions, which are lower by 50% for SCIAMACHY and 30% for OMI than the INTEX-B inventory. Thus, the reduction of 33.5% in the top-down China SO_2 emissions of this work can be interpreted by the joint contribution of a decrease trend and a possible overestimation in INTEX-B bottom-up inventory.

5.2. NH_3

[40] The NH_3 emissions over China have not changed much since 2000, as confirmed by the REAS inventory [*Ohara et al*., 2007]. Our study shows an overall decrease of 34.5% in the optimized from the TRACE-P 2000 inventory [*Streets et al*., 2003], which may indicate an overestimation in the TRACE-P inventory. As shown in Table 4, the total amount of the constrained NH_3 emission (0.72 Tg Mon^{-1}) for April 2008 is quite close to a recent bottom-up estimates (0.71 Tg Mon^{-1}) by *Huang et al*. [2012]. *Huang et al*. [2012] also pointed out that the TRACE-P 2000 inventory significantly overestimates the NH_3 emission by applying an overestimated emission factor across the whole country.

5.3. NO_x

[41] *Lin et al*. [2010] constrained Chinese anthropogenic emissions of NO_x July 2008 with tropospheric NO_2 retrievals from GOME-2 and OMI instruments. They found the top-down emissions are (10 – 15%) lower than the a priori near Beijing (in agreement with results from *Mijling et al*. [2009]), in the northeastern provinces and along the east coast; yet they exceed the a priori over many inland regions. Overall, they presented a best top-down estimate of annual NO_x production is 6.8 Tg N, or 22.34 Tg NO_2, which is slightly higher than a priori. While the change in NO_x emission over China remains a controversy, the 18.8% difference of posterior NO_x emissions from the bottom-up still lies in the ±31% uncertainty of the inventory [*Zhang et al*., 2009b]. We argue bottom-up NO_x estimate from INTEX-B inventory could have a possible overestimation.

5.4. BC and OC

[42] Major emitting sectors of BC and OC are coal and biofuel combustion by industry, residential, and transportation activities. The trend of BC and OC emissions in China during recent years are controlled by the balance between decrease in emission factor, which pertains to improved technology, and increase in coal and fuel consumptions. According to MEP-2008 [*Ministry of Environmental Protection*, 2009], the annual smoke emission in China decreased by about 17.2% from 2006 to 2008. While BC and OC emissions estimated by *Lu et al*. [2011] and *Zhao et al*. [2013] remain almost same between 2006 and 2008, *Qin and Xie* [2012] reported a 3.8% increase. The top-down BC emission is 0.10 Tg mon^{-1} (or 1.509 Tg yr^{-1} based on the monthly variation in INTEX-B inventory), which is smaller than that in INTEX-B, but close to estimates of 1.61 Tg yr^{-1} by *Qin and Xie* [2012] and1.68 Tg yr^{-1} by *Lu et al*. [2011]. In terms of China OC emission estimates for 2008, *Lu et al*. [2011] suggested a slightly larger value (3.37 Tg yr^{-1}), while *Zhao et al*. [2013] indicated a smaller value (2.8 Tg yr^{-1}) than INTEX-B (3.22 Tg yr^{-1}). Our OC emission estimate (0.18 Tg mon^{-1} or 2.92 Tg yr^{-1}) is within their reported range. It is noted that the uncertainty for OC emissions is reported to be very large: ±258% in INTEX-B [*Zhang et al*., 2009b], −43% to 80% by *Lu et al*. [2011], and −42% to 114% in a recent study by *Zhao et al*. [2013].

5.5. Mineral Dust

[43] The ~50% reduction in the posterior dust emission estimates suggests the use of DEAD mobilization scheme with GOCART source function possibly tends to produce a systematic positive bias over the Taklimakan and Gobi deserts regions over the northwestern China, even it works reasonably for the United States [*Fairlie et al*., 2007]. Similar results have been also found in top-down dust emission estimates by MODIS aerosol retrievals [*Wang et al*., 2012] and constrained dust emissions by surface PM measurements [*Ku and Park*, 2011]. Such overestimation by the dust mobilization scheme is also reflected through comparison GEOS-Chem AOD (as in Figure 6) and surface PM10 concentration (as in Figure 11) with in situ measurements near the dust source regions.

6. Discussions and Summary

[44] This study presents a two-stage inversion scheme to explore the capacity of using satellite radiance for inversion

of species-specific aerosol emissions. First, we prepare the observational constraints of AOD using an advanced aerosol retrieval algorithm, which integrates the GEOS-Chem aerosol optical properties to the MODIS observed radiance [*Wang et al*., 2010]. Second, the adjoint of the GEOS-Chem chemical transport model is applied to statistically optimize aerosol emission estimates using these AOD retrievals. Thus, the MODIS radiances are essentially used to optimize the estimates of the emitted aerosol tracers and precursors. We illustrate our concept first with an idealized numerical experiment and subsequently demonstrate the feasibility and practicability of the proposed scheme by applying it to optimize aerosol emission inventories over China during April 2008. Emissions of SO_2, NH_3, NO_x, BC, and OC from anthropogenic sources, which significantly influence the aerosol simulation, are selected to be constrained at a spatial resolution of $2^\circ \times 2.5^\circ$ and a monthly temporal resolution. Mineral dust production from combined natural and disturbed sources is optimized at the same spatial resolution but with a daily temporal resolution. Independent observations from both satellite remote sensing and ground-based observations are used to assess the inversion results through their comparisons with relevant GEOS-Chem simulations using prior and posterior emission estimates.

[45] The inversion yields posterior best estimates of 1.73 Tg for SO_2, 0.72 Tg for NH_3, 1.38 Tg for NO_x, 0.10 Tg for BC, and 0.18 for OC from anthropogenic sources, and 8.3 Tg for combined natural and disturbed mineral dust. These show notable decreases from their counterparts in the bottom-up inventories in amount (or percentage decrease): 0.87 Tg (33.5%) for SO_2, 0.38 Tg (34.5%) for NH_3, 0.32 Tg (18.8%) for NO_x, 0.01 Tg (9.1%) for BC, and 0.03 Tg (15.0%) for OC. The total amount of the mineral dust emission is reduced by 56.4% from 19.02 Tg simulated by the DEAD mobilization module. The distribution of emission scaling factors exhibits strong spatial variation for those anthropogenic-emitted tracers and considerable temporal variation for mineral dust. The use of top-down constrained emissions remarkably reduces the discrepancy between GEOS-Chem simulation and observational AOD constraints, in both spatial and temporal variation features.

[46] Resulting posterior estimates of emissions are evaluated with independent AOD observations from surface sites (AERONET) and satellite (MISR), SO_2 and NO_2 column retrievals from satellite (OMI), and surface SNA and PM_{10} concentrations from ground-based measurements. While the prior simulation over China generally shows overestimation, the use of posterior emissions significantly enhances the consistency between simulations and those independent observations. The statistical analysis of those comprehensive comparisons summarized in the Taylor diagram shows an overall reduced bias and RMS difference along with increased correlation coefficient, further confirming the improvements in the posterior simulation and the effectiveness of the presented top-down scheme.

[47] We attribute the differences between prior and posterior aerosol emissions to the change of emitted amount from the base year of those bottom-up inventories to the study period and/or the under/overestimations in those inventories. Through comparisons with emissions over China reported by recent studies, we find that our inversion results are consistent with following finding: (a) anthropogenic SO_2 emissions over China have been decreased by 5 – 10% from 2006 to 2008; (b) anthropogenic BC/OC emissions may be slightly reduced; (c) anthropogenic emissions of SO_2 and NO_x reported in the INTEX-B and NH_3 from TRACE-P inventories could have been artificially overestimated, (d) the DEAD mobilization scheme combined with GOCART dust source function, even works well over the United States [*Fairlie et al*., 2007], seems to simulate mineral dust surface fluxes with a systematic positive bias.

[48] As a first attempt to invert species-specific emissions with satellite radiance, this study has a number of limitations. Those limitations may impact the uncertainty in posterior emissions, which is supposed to be smaller than uncertainty characterizing either a priori or observational constraints [*Rodgers*, 2000]. While quantification of these is beyond the demonstrative purposes of this paper, we present a qualitative discussion as follows. First, in the stage of aerosol retrieval, we presume aerosol composition is unbiased and contains errors only in the total amount. As the model inevitably has bias associating aerosol types, improvement of this assumption over regional to global scale can be obtained from innovative satellite measurements. Indeed, the radiance observations have potential information on the aerosol composition. For example, the spectral behavior of the radiance is used to discriminate smoke from mineral dust particles [*King et al*., 1999; *Kaufman et al*., 2002]. Radiances measured from multiviewing angle are sensitive to aerosol particle size and nonsphericity [*Kahn et al*., 2005]. Temporal variation and geographical location can also yield information about aerosol composition. For example, increase of AOD in semi-arid region may reflect the increase of dust, while change of AOD in the Eastern Asia may reflect the increase of industrial emission. Hence, as shown in this study, a combined use of the model-based knowledge of the dominant aerosol sources and the source-receptor relationship together with the satellite-based temporal variation of AOD at different locations can be a strong constraint for species-specific source estimates. Second, this study also assumes the sole cause of the radiance difference (or the AOD difference) is due to the uncertainty in aerosol emissions. However, other processes can contribute to the difference, e.g., aerosol transport, wet/dry deposition, diurnal variation, prescribed aerosol physical and optical properties, and errors in the meteorological fields and radiative transfer calculation, etc. The third assumption is related to the error covariance matrices that are specified as diagonal with errors based upon literature (but that themselves may have uncertainty). To properly address these issues in future, a logical next step would be to assimilate multiple-spectral and/or multi-angle satellite radiance to the CTM. Furthermore, errors in the processes including emission, transport, and deposition and radiative transfer should be reasonably characterized and included in the optimization.

[49] The top-down inversion scheme using GEOS-Chem adjoint inverse modeling is a powerful tool to include observational constraints from different platforms for timely updating aerosol emissions. There is also a need of using combined tracer gas and aerosol measurements to simultaneously constrain the aerosol emissions and gas precursors. Encouraging results presented in this study reveal the potential of using aerosol observations from MODIS and MISR, SO_2 and NO_2 from OMI and other sensor, such as SCIAMACHY, in the

inversion. Inclusion of those observations will undoubtedly add more information to the optimization of emission.

[50] **Acknowledgments.** This research is supported by the NASA Radiation Sciences Program (for Glory mission) managed by Hal H. Maring, NASA Atmospheric Composition Program managed by Richard E. Eckman, and NASA New Investigator Program as well as a NASA Earth and Space Science Fellowship (to Xiaoguang Xu), both managed by Mingying Wei. We thank the data services provided by the Goddard Earth Science Data Center and the AERONET team in NASA GSFC, Jianping Huang from Lanzhou University (China) for providing the surface PM_{10} data, and the computational support provided by the Holland Computing Center of the University of Nebraska.

References

Benedetti, A., et al. (2009), Aerosol analysis and forecast in the European Centre for Medium-Range Weather Forecasts Integrated Forecast System: 2. Data assimilation, *J. Geophys. Res.*, *114*, D13205, doi:10.1029/2008JD011115.

Bey, I., D. J. Jacob, R. M. Yantosca, J. A. Logan, B. D. Field, A. M. Fiore, Q. Li, H. Y. Liu, L. J. Mickley, and M. G. Schultz (2001), Global modeling of tropospheric chemistry with assimilated meteorology: Model description and evaluation, *J. Geophys. Res.*, *106*(D19), 23,073–23,095.

Boersma, K. F., D. J. Jacob, H. J. Eskes, R. W. Pinder, J. Wang, and R. J. van der A (2008), Intercomparison of SCIAMACHY and OMI tropospheric NO_2 columns: Observing the diurnal evolution of chemistry and emissions from space, *J. Geophys. Res.*, *113*, D16S26, doi:10.1029/2007JD008816.

Bond, T. C., E. Bhardwaj, R. Dong, R. Jogani, S. Jung, C. Roden, D. G. Streets, and N. M. Trautmann (2007), Historical emissions of black and organic carbon aerosol from energy-related combustion, 1850–2000, *Global Biogeochem. Cycles*, *21*, GB2018, doi:10.1029/2006GB002840.

Borrego, C., A. I. Miranda, B. A. Roy, G. A. Pouliot, J. D. Mobley, T. G. Pace, T. E. Pierce, A. J. Soja, J. J. Szykman, and J. Al-Saadi (2008), Development of fire emissions inventory using satellite data, in *Air Pollution Modeling and Its Application XIX*, pp. 217–225, Springer Netherlands, Dordrecht, The Netherlands.

Bucsela, E. J., E. A. Celarier, M. O. Wenig, J. F. Gleason, J. P. Veefkind, K. F. Boersma, and E. J. Brinksma (2006), Algorithm for NO2 vertical column retrieval from the Ozone Monitoring Instrument, *IEEE Trans. Geosci. Remote Sens.*, *44*, 1245–1258.

Byrd, R. H., P. Lu, J. Nocedal, and C. Zhu (1995), A limited memory algorithm for bound constrained optimization, *SIAM J. Sci. Comput.*, *16*, 1190–1208.

Celarier, E. A., et al. (2008), Validation of Ozone Monitoring Instrument nitrogen dioxide columns, *J. Geophys. Res.*, *113*, D15S15, doi:10.1029/2007JD008908.

Drury, E., D. J. Jacob, J. Wang, R. J. D. Spurr, and K. Chance (2008), Improved algorithm for MODIS satellite retrievals of aerosol optical depths over western North America, *J. Geophys. Res.*, *113*, D16204, doi:10.1029/2007JD009573.

Drury, E., J. Jacob, R. J. D. Spurr, J. Wang, Y. Shinozuka, B. E. Anderson, A. D. Clarke, J. Dibb, C. McNaughton, and R. Weber (2010), Synthesis of satellite (MODIS), aircraft (ICARTT), and surface (IMPROVE, EPA-AQS, AERONET) aerosol observations over eastern North America to improve MODIS aerosol retrievals and constrain surface aerosol concentrations and sources, *J. Geophys. Res.*, *115*(D14), D14204.

Dubovik, O., T. Lapyonok, Y. J. Kaufman, M. Chin, P. Ginoux, R. A. Kahn, and A. Sinyuk (2008), Retrieving global aerosol sources from satellites using inverse modeling, *Atmos. Chem. Phys.*, *8*(2), 209–250.

Fairlie, D. T., D. J. Jacob, and R. J. Park (2007), The impact of transpacific transport of mineral dust in the United States, *Atmos. Environ.*, *41*(6), 1251–1266.

Forster, P., et al. (2007), Changes in atmospheric constituents and in radiative forcing, in *Climate Change 2007: The Physical Science Basis. Contribution of Working Group I to the Fourth Assessment Report of the Intergovernmental Panel on Climate Change*, edited by S. Solomon et al., pp. 129–234, Cambridge Univ. Press, Cambridge, U. K.

Fu, T. M., et al. (2012), Carbonaceous aerosols in China: Top-down constraints on primary sources and estimation of secondary contribution, *Atmos. Chem. Phys.*, *12*(5), 2725–2746.

Ge, J. M., J. Su, T. P. Ackerman, Q. Fu, J. P. Huang, and J. S. Shi (2010), Dust aerosol optical properties retrieval and radiative forcing over northwestern China during the 2008 China-U.S. joint field experiment, *J. Geophys. Res.*, *115*, D00K12, doi:10.1029/2009JD013263.

Ginoux, P., M. Chin, I. Tegen, J. M. Prospero, B. Holben, O. Dubovik, and S.-J. Lin (2001), Sources and distributions of dust aerosols simulated with the GOCART model, *J. Geophys. Res.*, *106*(D17), 20,255–20,273.

Hansen, P. C. (1998), *Rank-Deficient and Discrete Ill-Posed Problems: Numerical Aspects of Linear Inversion*, Soc. for Ind. and Appl. Math., Philadelphia, Pa.

Haywood, J., and O. Boucher (2000), Estimates of the direct and indirect radiative forcing due to tropospheric aerosols: A review, *Rev. Geophys.*, *38*(4), 513–543.

Heald, C. L., D. J. Jacob, D. B. A. Jones, P. I. Palmer, J. A. Logan, D. G. Streets, G. W. Sachse, J. C. Gille, R. N. Hoffman, and T. Nehrkorn (2004), Comparative inverse analysis of satellite (MOPITT) and aircraft (TRACE-P) observations to estimate Asian sources of carbon monoxide, *J. Geophys. Res.*, *109*, D23306, doi:10.1029/2004JD005185.

Heald, C. L., D. J. Jacob, R. J. Park, L. M. Russell, B. J. Huebert, J. H. Seinfeld, H. Liao, and R. J. Weber (2005), A large organic aerosol source in the free troposphere missing from current models, *Geophys. Res. Lett.*, *32*, L18809, doi:10.1029/2005GL023831.

Henze, D. K., A. Hakami, and J. H. Seinfeld (2007), Development of the adjoint of GEOS-Chem, *Atmos. Chem. Phys.*, *7*(9), 2413–2433.

Henze, D. K., J. H. Seinfeld, and D. T. Shindell (2009), Inverse modeling and mapping US air quality influences of inorganic PM2.5 precursor emissions using the adjoint of GEOS-Chem, *Atmos. Chem. Phys.*, *9*(16), 5877–5903.

Holben, B. N., et al. (1998), AERONET - A Federated Instrument Network and Data Archive for Aerosol Characterization, *Remote Sens. Environ.*, *66*(1), 1–16.

Huang, X., Y. Song, M. Li, J. Li, Q. Huo, X. Cai, T. Zhu, M. Hu, and H. Zhang (2012), A high-resolution ammonia emission inventory in China, *Global Biogeochem. Cycles*, *26*, GB1030, doi:10.1029/2011GB004161.

Huang, Z., J. Huang, J. Bi, G. Wang, W. Wang, Q. Fu, Z. Li, S.-C. Tsay, and J. Shi (2010), Dust aerosol vertical structure measurements using three MPL lidars during 2008 China-U.S. joint dust field experiment, *J. Geophys. Res.*, *115*, D00K15.

Jiang, Z., D. B. A. Jones, M. Kopacz, J. Liu, D. K. Henze, and C. Heald (2011), Quantifying the impact of model errors on top-down estimates of carbon monoxide emissions using satellite observations, *J. Geophys. Res.*, *116*, D15306, doi:10.1029/2010JD015282.

Kahn, R. A., B. J. Gaitley, J. V. Martonchik, D. J. Diner, K. A. Crean, and B. Holben (2005), Multiangle Imaging Spectroradiometer (MISR) global aerosol optical depth validation based on 2 years of coincident Aerosol Robotic Network (AERONET) observations, *J. Geophys. Res.*, *110*, D10S04, doi:10.1029/2004JD004706.

Kaufman, Y. J., D. Tanre, and O. Boucher (2002), A satellite view of aerosols in the climate system, *Nature*, *419*, 215–223.

King, M. D., Y. J. Kaufman, D. Tanre, and T. Nakajima (1999), Remote sensing of tropospheric aerosols from space: Past, present, and future, *Bull. Am. Meteorol. Soc.*, *80*(11), 2229–2259.

Kopacz, M., D. J. Jacob, D. K. Henze, C. L. Heald, D. G. Streets, and Q. Zhang (2009), Comparison of adjoint and analytical Bayesian inversion methods for constraining Asian sources of carbon monoxide using satellite (MOPITT) measurements of CO columns, *J. Geophys. Res.*, *114*, D04305, doi:10.1029/2007JD009264.

Kopacz, M., et al. (2010), Global estimates of CO sources with high resolution by adjoint inversion of multiple satellite datasets (MOPITT, AIRS, SCIAMACHY, TES), *Atmos. Chem. Phys.*, *10*(3), 855–876.

Kopacz, M., D. L. Mauzerall, J. Wang, E. M. Leibensperger, D. K. Henze, and K. Singh (2011), Origin and radiative forcing of black carbon transported to the Himalayas and Tibetan Plateau, *Atmos. Chem. Phys.*, *11*(6), 2837–2852.

Krotkov, N. A., S. A. Carn, A. J. Krueger, P. K. Bhartia, and K. Yang (2006), Band residual difference algorithm for retrieval of SO2 from the Aura Ozone Monitoring Instrument (OMI). *IEEE Trans.Geosci. Remote Sens.*, *44*(5), 1259–1266.

Ku, B., and R. J. Park (2011), Inverse modeling analysis of soil dust sources over East Asia, *Atmos. Environ.*, *45*(32), 5903–5912.

Lamsal, L. N., R. V. Martin, A. Padmanabhan, A. van Donkelaar, Q. Zhang, C. E. Sioris, K. Chance, T. P. Kurosu, and M. J. Newchurch (2011), Application of satellite observations for timely updates to global anthropogenic NO*x* emission inventories, *Geophys. Res. Lett.*, *38*, L05810, doi:10.1029/2010GL046476.

Lee, C., R. V. Martin, A. van Donkelaar, G. O'Byrne, N. Krotkov, A. Richter, L. G. Huey, and J. S. Holloway (2009), Retrieval of vertical columns of sulfur dioxide from SCIAMACHY and OMI: Air mass factor algorithm development, validation, and error analysis, *J. Geophys. Res.*, *114*, D22303, doi:10.1029/2009JD012123.

Lee, C., R. V. Martin, A. van Donkelaar, H. Lee, R. R. Dickerson, J. C. Hains, N. Krotkov, A. Richter, K. Vinnikov, and J. J. Schwab (2011), SO2 emissions and lifetimes: Estimates from inverse modeling using in situ and global, space-based (SCIAMACHY and OMI) observations, *J. Geophys. Res.*, *116*, D06304, doi:10.1029/2009JD012123.

Levy, R. C., L. A. Remer, R. G. Kleidman, S. Mattoo, C. Ichoku, R. Kahn, and T. F. Eck (2010), Global evaluation of the Collection 5 MODIS dark-target aerosol products over land, *Atmos. Chem. Phys.*, *10*(21), 10,399–10,420.

Lin, J. T., M. B. McElroy, and K. F. Boersma (2010), Constraint of anthropogenic NOx emissions in China from different sectors: A new methodology using multiple satellite retrievals, *Atmos. Chem. Phys.*, *10*(1), 63–78.

Liu, H., D. J. Jacob, I. Bey, and R. M. Yantosca (2001), Constraints from ^{210}Pb and ^{7}Be on wet deposition and transport in a global three-dimensional chemical tracer model driven by assimilated meteorological fields, *J. Geophys. Res.*, *106*, 12,109–12,128.

Liu, Y., J. A. Sarnat, V. Kilaru, D. J. Jacob, and P. Koutrakis (2005), Estimating ground-level PM2.5 in the eastern United States using satellite remote sensing, *Environ. Sci. Technol.*, *39*(9), 3269–3278.

Lu, Z., D. G. Streets, Q. Zhang, S. Wang, G. R. Carmichael, Y. F. Cheng, C. Wei, M. Chin, T. Diehl, and Q. Tan (2010), Sulfur dioxide emissions in China and sulfur trends in East Asia since 2000, *Atmos. Chem. Phys.*, *10*(13), 6311–6331.

Lu, Z., Q. Zhang, and D. G. Streets (2011), Sulfur dioxide and primary carbonaceous aerosol emissions in China and India, 1996–2010, *Atmos. Chem. Phys.*, *11*(18), 9839–9864.

Martin, R. V., D. J. Jacob, K. Chance, T. P. Kurosu, P. I. Palmer, and M. J. Evans (2003), Global inventory of nitrogen oxide emissions constrained by space-based observations of NO2 columns, *J. Geophys. Res.*, *108*(D17), 4537, doi:10.1029/2003JD003453.

Mijling, B., K. F. Boersma, M. V. Roozendael, I. DeSmedt, and H. M. Kelder (2009), Reductions of NO2 detected from space during the 2008 Beijing Olympic Games, *Geophys. Res. Lett.*, *36*, L13801, doi:10.1029/2009GL038943.

Ministry of Environmental Protection (2009), *Report on the state of the environment in China 2008*, Beijing.

Müller, J. F., and T. Stavrakou (2005), Inversion of CO and Nox emissions using the adjoint of the IMAGES model, *Atmos. Chem. Phys.*, *5*(5), 1157–1186.

Nassar, R., et al. (2011), Inverse modeling of CO2 sources and sinks using satellite observations of CO2 from TES and surface flask measurements, *Atmos. Chem. Phys.*, *11*(2), 6029–6047.

Ohara, T., H. Akimoto, J. Kurokawa, N. Horii, K. Yamaji, X. Yan, and T. Hayasaka (2007), An Asian emission inventory of anthropogenic emission sources for the period 1980–2020, *Atmos. Chem. Phys.*, *7*(16), 4419–4444.

Park, R. J., D. J. Jacob, B. D. Field, R. M. Yantosca, and M. Chin (2004), Natural and transboundary pollution influences on sulfate-nitrate-ammonium aerosols in the United States: Implications for policy, *J. Geophys. Res.*, *109*, D15204, doi:10.1029/2003JD004473.

Parrington, M., et al. (2012), The influence of boreal biomass burning emissions on the distribution of tropospheric ozone over North America and the North Atlantic during 2010, *Atmos. Chem. Phys.*, *12*, 2077–2098.

Pope, C. A., M. Ezzati, and D. W. Dockery (2009), Fine-particulate air pollution and life expectancy in the United States, *N. Engl. J. Med.*, *360*(4), 376–386.

Qin, Y., and S. D. Xie (2012), Spatial and temporal variation of anthropogenic black carbon emissions in China for the period 1980–2009, *Atmos. Chem. Phys.*, *12*(11), 4825–4841.

Reid, J. S., et al. (2009), Global monitoring and forecasting of biomass-burning smoke: Description of and lessons from the Fire Locating and Modeling of Burning Emissions (FLAMBE) program, *Sel. Top. Appl. Earth Observ. Remote Sens., IEEE J.*, *2*(3), 144–162.

Remer, L. A., et al. (2005), The MODIS aerosol algorithm, products, and validation, *J. Atmos. Sci.*, *62*(4), 947–973.

Rodgers, C. D. (2000), *Inverse Methods for Atmospheric Sounding: Theory and Practice*, World Sci., Singapore.

Schulz, M., et al. (2006), Radiative forcing by aerosols as derived from the AeroCom present-day and pre-industrial simulations, *Atmos. Chem. Phys.*, *6*(12), 5225–5246.

Seinfeld, J. H. and Pandis, S. N. (1998), *Atmospheric Chemistry and Physics – From Air Pollution to Climate Change*, 1326 pp., John Wiley, New York.

Sinyuk, A., et al. (2008), Multi-sensor aerosol retrievals using joint inversion of AERONET and satellite observations: Concept and applications, *Eos Trans. AGU*, *89*(53), Fall Meet. Suppl., Abstract A23B-0287.

Spurr, R. (2006), VLIDORT: A linearized pseudo-spherical vector discrete ordinate radiative transfer code for forward model and retrieval studies in multilayer multiple scattering media, *J. Quant. Spectrosc. Radiat. Transfer*, *102*, 316–342.

Stavrakou, T., and J. F. Müller (2006), Grid-based versus big region approach for inverting CO emissions using Measurement of Pollution in the Troposphere (MOPITT) data, *J. Geophys. Res.*, *111*, D15304, doi:10.1029/2005JD006896.

Streets, D. G., et al. (2003), An inventory of gaseous and primary aerosol emissions in Asia in the year 2000, *J. Geophys. Res.*, *108*(D21), 8809, doi:10.1029/2002JD003093.

Streets, D. G., Q. Zhang, L. Wang, K. He, J. Hao, Y. Wu, Y. Tang, and G. R. Carmichael (2006), Revisiting China's CO emissions after the Transport and Chemical Evolution over the Pacific (TRACE-P) mission: Synthesis of inventories, atmospheric modeling, and observations, *J. Geophys. Res.*, *111*, D14306, doi:10.1029/2006JD007118.

Taylor, K. E. (2001), Summarizing multiple aspects of model performance in a single diagram, *J. Geophys. Res.*, *106*(D7), 7183–7192.

Textor, C., et al. (2006), Analysis and quantification of the diversities of aerosol life cycles within AeroCom, *Atmos. Chem. Phys.*, *6*(7), 1777–1813.

Walker, T. W., et al. (2010), Trans-Pacific transport of reactive nitrogen and ozone to Canada during spring, *Atmos. Chem. Phys.*, *10*(17), 8353–8372.

Wang, Y., D. J. Jacob, and J. A. Logan (1998), Global simulation of tropospheric O3-NOx-hydrocarbon chemistry: 1. Model formulation, *J. Geophys. Res.*, *103*(D9), 10,713-10,72.

Wang, J., U. Nair, and S. A. Christopher (2004), GOES-8 Aerosol optical thickness assimilation in a mesoscale model: Online integration of aerosol radiative effects, *J. Geophys. Res.*, *109*, D23203, doi:10.1029/2004JD004827.

Wang, J., S. A. Christopher, U. S. Nair, J. S. Reid, E. M. Prins, J. Szykman, and J. L. Hand (2006), Mesoscale modeling of Central American smoke transport to the United States: 1. "Top-down" assessment of emission strength and diurnal variation impacts, *J. Geophys. Res.*, *111*, D05S17, doi:10.1029/2005JD006416.

Wang, J., X. Xu, R. Spurr, Y. Wang, and E. Drury (2010), Improved algorithm for MODIS satellite retrievals of aerosol optical thickness over land in dusty atmosphere: Implications for air quality monitoring in China, *Remote Sens. Environ.*, *114*(11), 2575–2583.

Wang, J., X. Xu, D. K. Henze, J. Zeng, Q. Ji, S.-C. Tsay, and J. Huang (2012), Top-down estimate of dust emissions through integration of MODIS and MISR aerosol retrievals with the GEOS-Chem adjoint model, *Geophys. Res. Lett.*, *39*, L08802, doi:10.1029/2012GL051136.

Weaver, C., A. da Silva, M. Chin, P. Ginoux, O. Dubovik, D. Flittner, A. Zia, L. Remer, B. Holben, and W. Gregg (2007), Direct insertion of MODIS radiances in a global aerosol transport model, *J. Atmos. Sci.*, *64*(3), 808–827.

Wecht, K. J., D. J. Jacob, S. C. Wofsy, E. A. Kort, J. R. Worden, S. S. Kulawik, D. K. Henze, M. Kopacz, and V. H. Payne (2012), Validation of TES methane with HIPPO aircraft observations: Implications for inverse modeling of methane sources, *Atmos. Chem. Phys.*, *12*, 1823–1832.

van Donkelaar, A., R. V. Martin, and R. J. Park (2006), Estimating ground-level PM2.5 using aerosol optical depth determined from satellite remote sensing, *J. Geophys. Res.*, *111*, D21201, doi:10.1029/2005JD006996.

van Donkelaar, A., et al. (2008), Analysis of aircraft and satellite measurements from the Intercontinental Chemical Transport Experiment (INTEX-B) to quantify long-range transport of East Asian sulfur to Canada, *Atmos. Chem. Phys.*, *8*(11), 2999–3014.

van der Werf, G. R., J. T. Randerson, L. Giglio, G. J. Collatz, P. S. Kasibhatla, and A. F. Arellano Jr (2006), Interannual variability in global biomass burning emissions from 1997 to 2004, *Atmos. Chem. Phys.*, *6*(11), 3423–3441.

van der Werf, G. R., J. T. Randerson, L. Giglio, G. J. Collatz, M. Mu, P. S. Kasibhatla, D. C. Morton, R. S. DeFries, Y. Jin, and T. T. van Leeuwen (2010), Global fire emissions and the contribution of deforestation, savanna, forest, agricultural, and peat fires (1997–2009), *Atmos. Chem. Phys.*, *10*(23), 11707–11735.

Wesely, M. L. (1989), Parameterization of surface resistance to gaseous dry deposition in regional-scale numerical models, *Atmos. Environ.*, *23*, 1293–1304.

Zender, C. S., H. Bian, and D. Newman (2003), Mineral Dust Entrainment and Deposition (DEAD) model: Description and 1990s dust climatology, *J. Geophys. Res.*, *108*(D14), 4416, doi:10.1029/2002JD002775.

Zhang, J., J. S. Reid, D. L. Westphal, N. L. Baker, and E. J. Hyer (2008), A system for operational aerosol optical depth data assimilation over global oceans, *J. Geophys. Res.*, *113*, D10208, doi:10.1029/2007jd009065.

Zhang, L., S. Gong, J. Padro, and L. Barrie (2001), A size-segregated particle dry deposition scheme for an atmospheric aerosol module, *Atmos. Environ.*, *35*, 549–560.

Zhang, L., D. J. Jacob, M. Kopacz, D. K. Henze, K. Singh, and D. A. Jaffe (2009a), Intercontinental source attribution of ozone pollution at western U.S. sites using an adjoint method, *Geophys. Res. Lett.*, *36*, L11810, doi: 10.1029/2009GL037950.

Zhang, Q., et al. (2009b), Asian emissions in 2006 for the NASA INTEX-B mission, *Atmos. Chem. Phys.*, *9*(14), 5131–5153.

Zhao, Y., J. Zhang, and C. P. Nielsen (2013), The effects of recent control policies on trends in emissions of anthropogenic atmospheric pollutants and CO2 in China, *Atmos. Chem. Phys.*, *13*(2), 487–508.

Zoogman, P., D. J. Jacob, K. Chance, L. Zhang, P. Le Sager, A. M. Fiore, A. Eldering, X. Liu, V. Natraj, S. S. Kulawik (2011), Ozone air quality measurement requirements for a geostationary satellite mission, *Atmos. Environ.*, *45*, 7143–7150.